Chapter 2

A SEARCH FOR INFLUENCES OF TIDAL STRESSES ON SURFACE FEATURE FORMATION ON IO

Christina Seeger[1] & Katherine de Kleer[1]

"So have I seen Passion and Vanity stamping the living magnanimous earth, but the earth did not alter her tides and her seasons for that."

Moby Dick, Chapter 48: The First Lowering

Abstract

Mountains and paterae are distinctive features on the surface of Io whose relationship to each other and formation mechanisms have been the subject of long debate. Though mountain formation likely stems from much deeper in the crust than the ultimate exit of magma onto the surface in the form of depressed paterae, both feature types exhibit distinctive elongate shapes, and in the case of paterae, a characteristic planform aspect ratio of 2:3 (short:long axis). We present the first investigation into whether tidal stresses may play a role in the formation of these features on the surface by modeling the maximum compressive and tensional tidal stress experienced at each mountain and patera location throughout Io's orbit, and comparing it to the orientation of the feature on the surface, hypothesizing that tensional stress in one direction may result in a perpendicularly-oriented patera, and compression could produce perpendicular mountains. While we found no significant perpendicular relationships between features and stresses, mountains are significantly likely to form ~30° or ~60° offset from the orientation of the maximum compressive stress vector at that location. The paterae, in contrast, have a weakly nonuniform offset from stress, but without a dominant preferred orientation. The strongest relationships discovered relate to regional trends in orientation: paterae in the subjovian hemisphere are highly unlikely to be oriented NE-SW,

[1] Division of Geological and Planetary Sciences, California Institute of Technology, Pasadena, CA 91125, USA.

while the antijovian hemisphere is statistically uniform in orientation; we suggest the presence of Loki Patera may influence the formation of proximal paterae due to subsurface magma movement.

1. Introduction

Io is a world of intense volcanism, driven by its eccentric orbit forced by resonance with Europa and Ganymede (Peale et al., 1979). Tidal stresses resulting from this eccentric orbit frictionally heat Io's interior, melting it enough to frequently and powerfully expel lava onto the surface in dramatic volcanic eruptions that occur so frequently they resurface the moon at a rate of ~ 0.1-1 centimeter per year (Carr et al., 1998; Geissler et al., 2004; Johnson et al., 1979). Over geologic time, the flows create layers of basaltic to possibly ultramafic crust, interbedded with sulfur-rich deposits and sulfur dioxide frost, that is estimated to be 13-30 kilometers thick (Jaeger et al, 2003; Kirchoff & McKinnon, 2009; Schenk et al., 2001). This layered crust is compressed continuously under deep crustal subsidence stresses that are accommodated in the lithosphere by intense subsurface faulting, which can give rise to a suite of imposing up-thrust tectonic mountains in the form of stepped plateaus and tilted blocks rising up to 16 kilometers high (McEwen et al., 2004; McKinnon et al., 2001; Schenk & Bulmer 1998; Schenk et al., 2001; Turtle et al., 2001). Unlike on Earth, where long mountain chains form due to plate movements, Io's mountains form as tall, isolated, usually elongate massifs rising abruptly from the smooth plains below like islands (e.g., Schenk et al, 2001; Turtle et al., 2001; Williams et al., 2011).

Eruptions are centered around paterae, which are depressed caldera-like features with steep walls, flat floors, and arcuate margins, and often have lava flows extending outwards from them (Radebaugh et al., 2001). Thermal emission from these volcanic eruptions is easily detectable from both spacecraft and ground-based observing on Earth (Davies et al., 2001; 2010; 2024; de Kleer et al., 2019a; de Pater, et al., 2017; Lopes et al., 2001; McEwen et al., 1998; Perry et al., 2024; Veeder et al., 1994). The formation and eruptive mechanisms for paterae are not entirely understood, but hypothesized models include magma rising from either the aesthenosphere or a magma ocean to feed isolated magma chambers and crustal intrusions that can eventually exploit the tectonically fractured subsurface to rise to the surface (Davies et al., 2006; Jaeger et al., 2003; Keszthelyi et al., 2004; Spencer et al., 2020). Alternatively, eruptions may be fed by hot-spot type volcanism, where magma ascends through crustal weaknesses in a heat-pipe regime (Keszthelyi et al., 2004; 2007; Kirchoff & McKinnon, 2009; McKinnon et al., 2001; O'Reilly & Davies, 1981). The presence or absence of an interconnected subsurface melt layer is poorly constrained, but has implications for the eruptive patterns at paterae and also the dissipation of tidal stresses throughout Io. The absence of such a layer requires heat dissipation through solid crust, meaning volcanic activity would likely correlate with heating centers. A melt layer, however, allows heat to be redistributed laterally, and volcanoes can form away from regions of increased tidal heating. Recent observations from the *Juno* spacecraft help constrain Io's interior, suggesting that a magma ocean is unlikely (Park et al., 2024) but a thin magma ocean at a depth of ~>250 km is still compatible with observations (Aygün & Čadek, 2025). While it is not yet well understood which of these mechanisms is dominant in forming these surface features, it is possible (even probable) that there many mechanisms driving the formation of these features.

Previous studies have attempted to constrain the relationship between mountains and paterae. On a global scale, mountains and paterae are statistically anticorrelated, concentrated in opposite hemispheres offset 90 degrees from each other with two significant groups of paterae clustered near the subjovian and antijovian points (Hamilton et al., 2013; Kirchoff et al., 2010; Radebaugh et al., 2001; Schenk et al., 2001; Tackley et al., 2001; Veeder et al., 2012). However, there are also many local examples of mountain/paterae associations (e.g., Ahern et al., 2017; Carr et al., 1998; Jaeger et al., 2003; Turtle et al., 2001), with examples suggesting patera formation can occur as mountains are rifted apart (Bunte et al., 2010; Seeger et al., 2025). No previous studies have identified a mechanism for influencing the orientation of mountains and paterae on the surface in a preferential way. An intuitive relationship is that of compressive stresses uplifting mountains perpendicular to the direction of principle stress, and tensile stresses rifting the crust orthogonal to the stresses.

In this study, we consider the time-varying compressional and tensile stresses from tides, which have a precedent for controlling volcanic activity (e.g., de Kleer et al., 2019). These phenomena are not limited to Io: Enceladus' plumes have characteristic timing, and on Earth, certain volcanoes like Mount Etna and Mount Ruapehu show sensitivity to tidal forces near eruption time (Běhounková et al., 2015; Hedman et al., 2013; Hurford et al., 2007; Sottili & Palladino, 2012; Girona et al., 2018). Io's own Loki Patera shows a ~460 day cycle that may be linked to periodic variations in Io's eccentricity caused by forcing from Europa and Ganymede (de Kleer er al., 2019). Tidal influence on Io's surface features has precedent, albeit on a much thinner layer of crust that may be more responsive to outside forcing: Bart et al. (2004) demonstrated small-scale ridges on the kilometer scale had alignment with the tidal stress field, suggesting they formed from tidal flexing. Therefore, by mapping the elongate compressional (mountains) and extensional (paterae) surface features globally and comparing their orientations to the tidal stresses they experience each orbit, this study constrains the influence of tidal stresses on the formation and expression of these features across the surface of Io.

2. Methods

2.1 Feature Mapping

Previous mapping efforts by Williams et al. (2011) outlined the extent of mountains and paterae on the surface of Io, using the USGS global basemap of Io (Williams et al., 2011). We used this geologic map, in concert with the 1 km/pixel global basemap of Io derived from *Voyager* and *Galileo* imagery, and the 15% of the surface that was imaged by *Galileo* at a higher resolution of 500 m/pixel or better. We use the publicly available Williams et al. (2021) database for the mosaiced *Voyager*/*Galileo* imagery as a basemap and geologic map shapefiles, using ESRI ArcGIS Pro™ software. The published geologic map contains 140 mountains, 172 hot spots based on thermal observations, and 432 paterae.

Paterae often contain multiple unit types within a singular feature (both bright and dark patera floor material, for example), so polygons of different unit types within each patera were merged into a single "patera" polygon using the Dissolve Tool (leaving "multipart features" and "unsplit lines" unchecked); three features severed by the central meridian were also merged, resulting in a total of 430 paterae (Figure 1) Similarly, mountains with multiple components (lineated, mottled, or undivided) were merged together and "Layered Plains" units were excluded based on the Unit field, resulting in a total of 120 mountains in the dataset (Figure 1).

The basemap is often presented using a simple cylindrical map projection, which preserves angles but distorts shapes and areas of features, especially at high latitudes. Care must be taken to ensure the shapes of paterae and mountains are not misinterpreted as elongate due to map projection distortion. Distortions of distances, areas, or angles can introduce considerable error in measurements made in planetary contexts. Kneissl et al. (2011) present a methodology to eliminate measurement distortion and create map-projection-independent crater size-frequency distributions for age dating, which requires that each crater be reprojected into a stereographic map projection centered on the center point of the crater. Terrestrial maps with stereographic projections are most commonly used over polar regions or small continents like Australia, where the map is conformal; though extreme distortions occur at the periphery, in the center, shapes are well preserved, directions are true, and lines drawn through the center point are great circles, meaning length and width measurements are geodesic and unaffected by the map projection. Therefore, in order to accurately measure the length, width, and resulting aspect ratio of each patera and mountain on Io, the map (using the standard GCG Io 2000 geographic coordinate system) was reprojected to a Stereographic (Sphere) projection using the polygon's midpoint latitude and longitude as the center parallel and meridian of the projection. While projected, we then ran the Minimum Bounding Geometry—Rectangle by Width tool to create a rectangle best representing the length and width of the feature, as well as the orientation from North of the long axis.

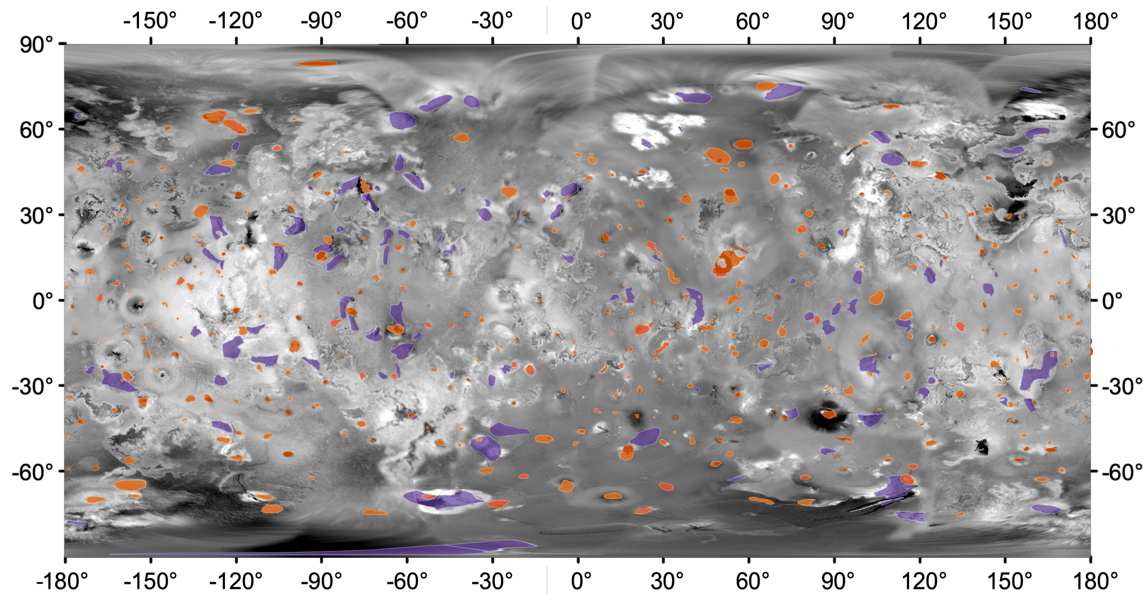

Figure 1. Map of locations of paterae (orange) and mountains (purple) used in this study, derived from USGS geologic units shapefiles. Combined *Voyager/Galileo* basemap and polygons are presented in a simple cylindrical projection centered on the subjovian point (0°W). Longitudes are given in 0-180° format, east positive.

2.2 Tidal Modelling

Io's orbital resonance with Europa and Ganymede produces an eccentric orbit, which results in diurnal tidal stresses in the crust that change in magnitude and orientation throughout its ~42.5 hour orbit around Jupiter (e.g., Peale et al., 1979; Ross & Schubert, 1985; Ross et al., 1990; Segatz et al., 1988). These stresses can be modeled with the open-source 2D numerical program software SatStressGUI, which calculates the compression and tension experienced at each point on the surface throughout a single orbit (Kay & Kattenhorn, 2010; Patthoff et al., 2016). SatStressGUI, and its predecessor SatStress (Wahr et al., 2009) uses a four-layer viscoelastic satellite model consisting of two-part lithosphere (a rigid upper lithosphere (Layer 1 or L1) and ductile lower lithosphere (L2)), ductile asthenosphere (L3), and combined mantle and core (L4), and has been used widely to model tidal stresses on Europa and other moons (e.g., Beuthe, 2015; Groenleer & Kattenhorn, 2008; Jara-Orué & Vermeersen, 2011; Olgin et al., 2011; Smith-Konter & Pappalardo, 2008). The model was adapted to Io by adjusting the input parameters to match a range of assumptions about Io's interior composition based on ground-based and spacecraft observations. These input parameters include mass of Jupiter, eccentricity of Io's orbit (0.0041, Greenberg, 1982), obliquity (0.002, Baland et al., 2012), semimajor axis (4.21 x 108 m), and the density, thickness, viscosity, Young's Modulus, and Poisson's ratio of each layer (Table 1), modeled after Patthoff & Davies (2017). Because the properties of Io's interior are poorly constrained and the presence of an interconnected melt layer has been debated until recent observations precluded a shallow melt layer (e.g., Aygün & Čadek, 2025; Khurana, et al., 2011; Park et al., 2025), a range of values were tested and stresses were modeled for both the presence and absence of a global magma ocean. To model a case with no ocean layer, we make L2 extremely thick, thus negating the effects of the L3 layer on L1 and L2; this method has been used previously for (possible) ocean worlds (e.g., Rhoden et al., 2015; 2017). The thin liquid layer of L3 decouples the mantle and core from the lithosphere layers such that they have a negligible effect on tidal stresses on the surface (Rhoden et al., 2017 showed the L4 contribution to the magnitude of tidal stresses to be <1%).

Table 1. Range of input parameters tested for tidal model in SatStressGUI. Bold values in parentheses are values used for model case with no magma ocean used to calculate stress orientations for the remainder of results.

Layer	Density (kg/m3) (x1000)	Young's Modulus (Pa)	Poisson's Ratio	Thickness (km)	Viscosity (Pa s)
L1: Upper Lithosphere	2.3 - 3.0 (**3.0**)	1 E9 - 1 E11 (**1 E11**)	0.2 - 0.3 (**0.2**)	5 - 50 (**5**)	1 E19 - 1 E26 (**1 E25**)
L2: Lower Lithosphere	2.5 - 3.2 (**3.2**)	1 E9 - 1 E11 (**1 E10**)	0.2 - 0.3 (**0.2**)	10 - 863 (**863**)	1 E9 - 1 E20 (**1 E14**)
L3: Asthenosphere	3.3 - 3.7 (**3.7**)	**0**	**0.5**	1 - 20 (**10**)	0 - 1 E6 (**1 E2**)
L4: Mantle + Core	4.5 - 6.0 (**5**)	1 E9 - 1 E12 (**1 E12**)	0.2 - 0.3 (**0.2**)	934 - 1806 (**944**)	**1 E4**

Though a range of input parameters were tested, including the presence and absence of a magma ocean, we found that changing parameters changed the amplitude of the resulting maximum compressive and tensile stresses, but changed the timing of peak diurnal stress by less than 30° in mean anomaly. Therefore, for the remainder of the study we focus only on the results from the case with no magma ocean, treating it as representative of the range of possible modeled results. Even if the timing and amplitude of some of these stresses are different for the different cases, the orientation of the *maximum* compressive and tensile stress is not changing significantly, which is the parameter we are using to compare to surface features. Stresses were modeled for every 10 degrees of mean anomaly (Figure 2). The magnitude-weighted average stress orientation was also calculated for each patera and mountain.

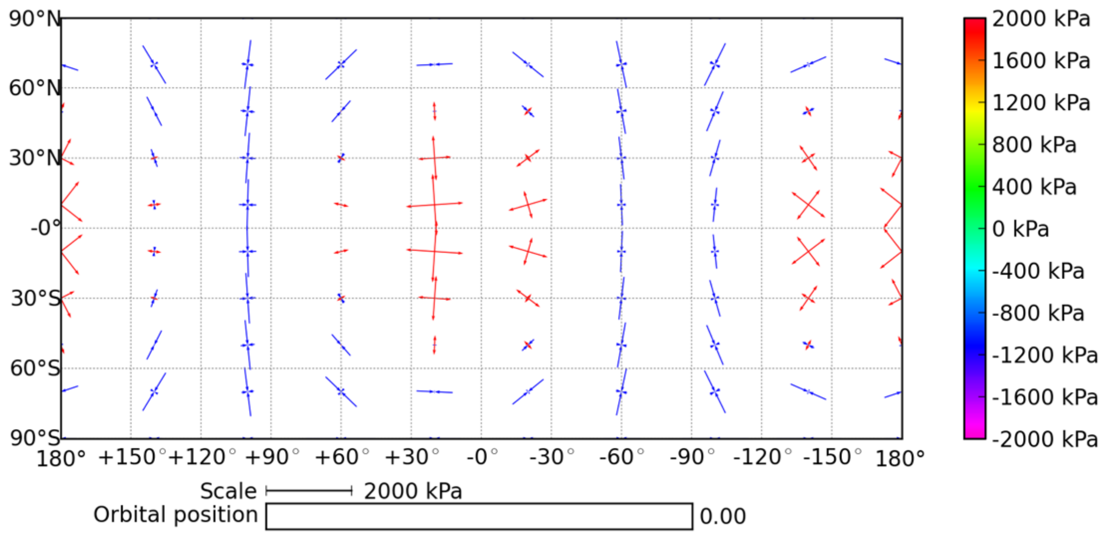

Figure 2. Map view of modeled diurnal tidal stresses calculated with SatStressGUI starting at periapsis and progressing in 30 degree increments until a full orbit is reached throughout animation. Stresses were modeled for three different conditions: no magma ocean (shown here, using bold parameters in Table 1), magma ocean with thin lithosphere, and magma ocean with thick lithosphere. Tension (red arrows) is positive.

From this global tidal stress modeling, we can then extract the tidal stresses modeled at the latitude and longitude location of each mountain and patera in the mapped dataset. The maximum compressional and extensional stress (and its orientation from north) experienced at each of these locations throughout Io's orbit were computed to compare to the orientations of the features.

2.3 Visual and Statistical Analysis

Rose diagrams, or circular histograms, are used across the field of Earth sciences to visualize directional data, from wind directions to fault orientations to paleomagnetic signatures, as well as throughout the solar system to map faults and straight crater rim segments (e.g., Cheng & Klimczak, 2025; Klimsczak et al., 2025). We generated rose diagrams for the measured orientations (East from North) of paterae and mountains produced with the Minimum Bounding Rectangle, as well as the orientations of the modeled maximum tensile (maximum σ_1) and maximum compressional (minimum σ_1) stresses experienced at the location of each feature during Io's orbit. Orientations are all measured 0-180° and are mirrored to better guide the eye. The difference between feature orientation and stress orientation was calculated from 0-180°, and then all differences above 90° were mirrored across the 90° axis to assess whether features were oriented parallel or perpendicular to the maximum tensile or compressional stress experienced; that is, a feature oriented 100° from the stress orientation is equivalent to being oriented 80° from the stress. Differences are plotted on a single quadrant rose diagram.

Rose diagrams are often plotted with the radius of each bin proportional to the frequency of the measurement, which can help our eyes pick out trends in the orientation data, but can be misleading in terms of how significant those trends are. A much more intuitive method is to plot equal-area rose diagrams, where the area of each bin is proportional to the frequency, rather than the radius, which is akin to plotting the square root of the frequency as the radial distance (Sanderson & Peacock, 2020). All rose diagrams are presented with a gray region representing a dataset of equal size with a uniform distribution of orientations for reference. Bin sizes were chosen using the widely adopted function recommended by Scott (1979), where the bin width in degrees (b) is related to the range (R; 180° in our case) and sample size (N) as $b = R / (2N^{1/3})$, rounding to the nearest common fraction of 180° for ease of plotting. This bin size function is favored because it is based on a normal distribution but avoids "over smoothing" (Sanderson & Peacock, 2020; Scott, 1979). For most of our datasets on order of N=100, we use a bin size of 15°, which is a reasonable value for the given sample sizes of the datasets; a bin size of 20° or 30° is used for the smaller subgroups of data. We create the polar histograms using the polar-projected bar plot function in the Python Matplotlib library (Hunter, 2007).

In order to quantitatively evaluate the distribution of the mapped feature orientations, we applied the Kuiper test for uniformity to determine if orientations or differences between feature and stress orientations have significant preferred orientations (Jammalamadaka & Sengupta, 2001, Kuiper, 1960; Landler et al., 2018). The Kuiper test is useful for directional data, and is based on the cumulative frequency without binning the data, and therefore can show departures from a uniform distribution without binning bias. The Kuiper test p-values were calculated using the Python-based Kuiper function in the astropy package (Price-Whelen et al., 2022). The null hypothesis is that orientations are randomly drawn from a uniform distribution; Kuiper test p-values less than an alpha level of 0.01 indicate there is a preferred orientation with 99% confidence. We chose a strict confidence interval due to testing a large number of subsets of the data. Using this test, we investigate two different hypotheses: Are patera or mountain orientations non-uniform on the surface? And is there a non-uniform relationship between those feature orientations and the orientation of maximum tensile or compressive stress they experience each orbit?

3. Orientation and Distribution of Features

3.1 Patera Shapes

Radebaugh et al. (2001) provide a comprehensive review of patera morphologies on Io and report that seventy percent of the global population of paterae have a planform aspect ratio of <0.8. This is consistent with our measurements, and our further exploration of the distribution of patera ellipticity reveals that paterae have a characteristic elongate shape, with a preferential aspect ratio of ~2/3. In our global survey of paterae, we found that 134 (31%) of paterae have an aspect ratio between 0.6-0.72 (Figure 3). The orientation of the long axis of the patera diminishes in significance for more circular paterae, so the dataset of "elongate" paterae used for the remainder of analyses is limited to those paterae with an aspect ratio <0.72, so defined because of the sharp shoulder in the patera shape distribution for features with an aspect ratio >0.72 (Figure 3).

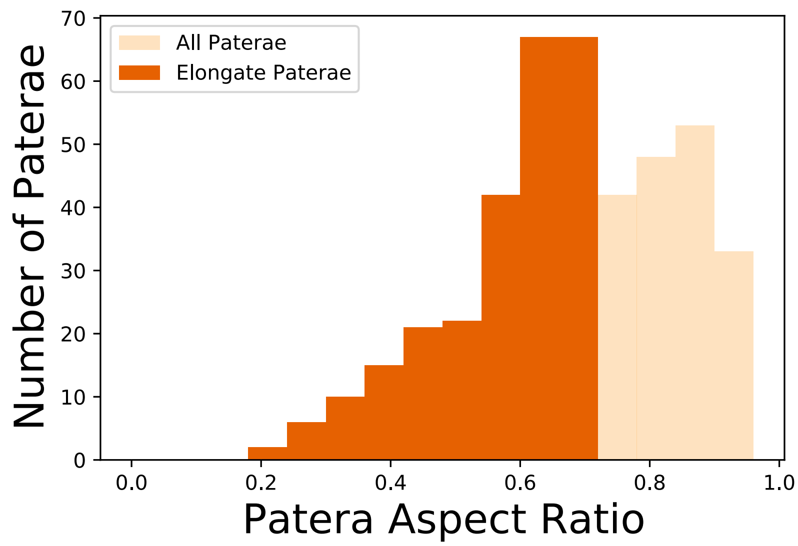

Figure 4. Distribution of patera shapes, both for full dataset of previously mapped paterae (N=430), and for the subset of paterae that are classified as "elongate" using an aspect ratio cutoff of 0.72 (exclusive) based on the peak in the aspect ratio distribution (N=252).

3.2 Patera Orientations

The long axis of each patera, as measured from a minimum bounding rectangle drawn around the feature using a stereographic projection centered on the feature midpoint, is oriented on the surface at some angle 0-180°, measured East from North where North = 0°. Because there is no directionality to the orientation data (an east-west oriented feature could have an orientation of 90° or 270° from north), we use equal-area polar histograms, or rose diagrams, with the orientations mirrored across the center of the circle in order to visualize the data. Using the Kuiper test for uniformity, we did not find that the elongate paterae (aspect ratio <0.72) significantly deviates from a uniform distribution of orientations (Table 2). To consider any regional trends, we divided the dataset to investigate the orientations of paterae in the entire northern and southern hemispheres, polar regions (latitude > ± 45°), equatorial region (latitude < ± 30°), sub- and antijovian hemispheres, and leading and trailing hemispheres (Figure 4). The Kuiper test did not return any *p*-values below the alpha level of 0.01 for any of these subdivisions except for the subjovian hemisphere, which returned a *p*-value of 0.0005, meaning that those paterae have non-uniform orientations with 99%

confidence (Table 2). These subjovian paterae do not have a unimodal preference, but rather are unlikely to be oriented NE/SW.

Table 2. Statistical significance of feature orientations and their relationship to the diurnal stress field, given as returned *p*-values from the Kuiper test of uniformity, subdivided by region. Mountain and patera orientations reflect the distribution of feature orientations where the long axis for features with planform aspect ratios <0.72 is measured east from north. Feature-Stress orientations reflect the absolute value of the difference between mountain or patera orientation and the orientation from north of maximum diurnal stress experienced by that feature each orbit.

Region	Number of Paterae	Patera Orientation	Patera-Stress Orientation	Number of Mountains	Mountain Orientation	Mountain-Stress Orientation
Global	252	0.1092	0.0583	93	0.1935	0.1354
Northern Hemisphere	122	0.9365	0.3541	47	0.0006	0.0068
Southern Hemisphere	130	0.0413	0.3154	46	0.6797	0.9081
North Pole	20	0.8121	0.8556	16	0.1172	0.3225
Equator	153	0.0974	0.111	47	0.3947	0.1907
South Pole	32	0.5927	0.1916	14	0.2378	0.0095
Subjovian Hemisphere	111	0.0005	0.0242	52	0.1312	0.032
Leading Hemisphere	118	0.4883	0.2878	56	0.2445	0.2122
Antijovian Hemisphere	141	0.8918	0.873	41	0.245	0.8811
Trailing Hemisphere	134	0.3831	0.3147	37	0.8423	0.6276

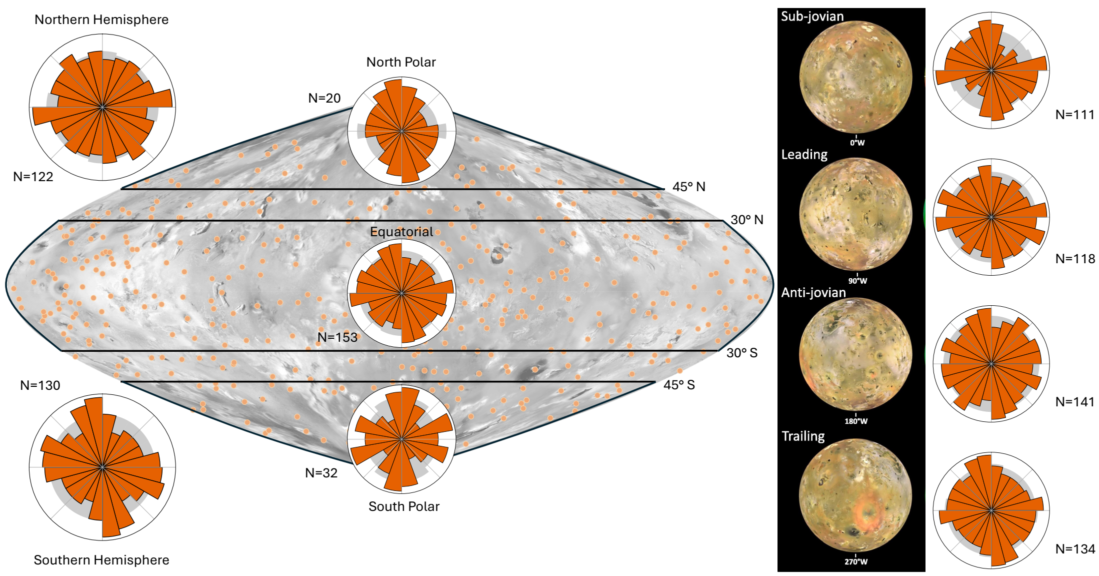

Figure 4. Orientations of long axes of elongate paterae across different regions of Io (those with an aspect ratio <0.72). North is up for all equal-area polar histograms, and orientations are measured from 0-180° and mirrored across the center of the circle The gray shaded region represents a uniform distribution for a dataset of the same size. A sinusoidal projection basemap centered on the subjovian point (0°W), with orange points corresponding to the locations of all paterae, is provided for reference. A larger bin size (20°) was used for the north and south polar rose plots due to smaller sample size, compared to 15° for all other plots.

3.3 Mountain Shapes

Unlike paterae, which have an irregular but often rounded shape, mountains tend to form as large, blocky massifs with a clear long axis. Therefore, the dataset of mountains used for this survey with aspect ratio <0.72 only excludes 27 mountains (or 22.5%) from those originally mapped (whereas 41% of paterae were excluded for being too circular). Though less pronounced than the patera shape distribution, mountains also have a characteristic shape with a large population having aspect ratios falling between 0.4-0.66 (Figure 5).

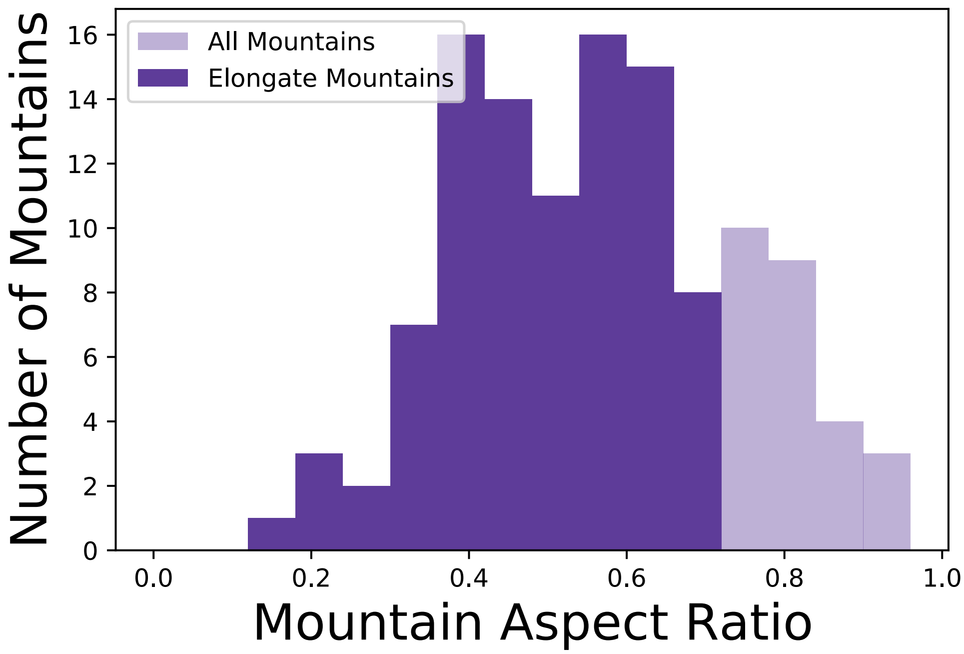

Figure 5. Distribution of mountain shapes, both for full dataset of previously mapped mountains (N=120), and for the subset of mountains that are visually elongate using the same aspect ratio cutoff of 0.72 that was used to classify paterae as "elongate" (N=93).

3.4 Mountain Orientations

We subdivide the dataset of elongate mountains by the same regions that were investigated for paterae: the entire northern and southern hemispheres, polar regions (latitude >45°), equatorial region (latitude <30°), sub- and antijovian hemispheres, and leading and trailing hemispheres (Figure 6). None of these subsets, nor the global dataset of elongate mountains (aspect ratio <0.72), can be shown to be non-uniform with the Kuiper test for uniformity, with the exception of the northern hemisphere, which returns a *p*-value of 0.006, meaning that northern mountains have a preferential orientation with 99% confidence (Table 2). These mountains are much more likely to be oriented N/NW-S/SE, and unlikely to be oriented E-W. Though the rest of the regional subdivisions do not show a significant deviation from uniform, the N/S preferential trend is visible in the subjovian and leading hemispheres as well.

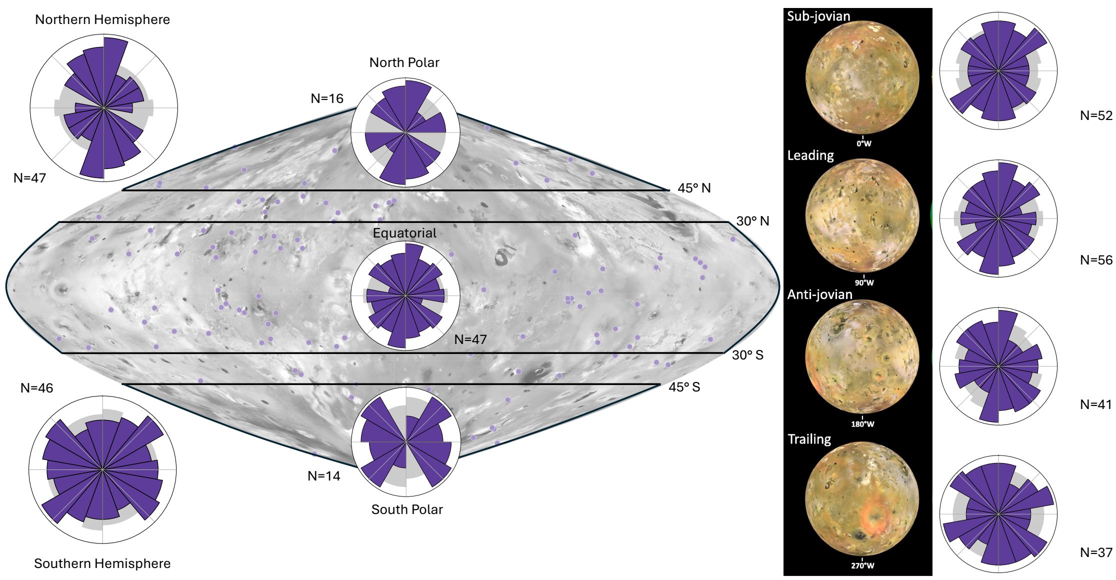

Figure 6. Orientations of long axes of elongate mountains across different regions of Io (those with an aspect ratio <0.72). North is up for all equal-area polar histograms, and orientations are measured from 0-180° and mirrored across the N-S meridian. The gray shaded region represents a uniform distribution for a dataset of the same size. A sinusoidal projection basemap centered on the subjovian point (0°W), with purple points corresponding to the locations of all mountains, is provided for latitudinal reference. For longitudinal reference, the USGS color mosaic has been orthographically re-projected to show the subjovian hemisphere (-90°–0°–90°), leading (-180°–0°), antijovian (90°–180°– -90°) and trailing (0°–180°) hemispheres of Io.

4. Tidal stresses and their relationship with feature orientation

4.1 Modeled stress results

Diurnal stresses were modeled using SatStressGUI, a four-layer viscoelastic model for orbital bodies (Kay & Kattenhorn, 2010; Patthoff et al., 2016; Wahr et al., 2009). The σ_1 and σ_3`stress components were calculated at the latitude and longitude of each patera and mountain midpoint through one orbit of Io around Jupiter, using a range of input parameters. These stress vectors have an amplitude, measured in kPa, and an orientation from north on the surface from 0-180°. We found that changing the thickness and density of each of the four layers in the model affected the amplitude of the stresses experienced, but not the timing or orientations of them. Therefore, all stresses presented in the following results are based on the input parameters for a case without a magma ocean, as presented in Table 1.

Each point on Io's surface experiences a rotating stress field with tension and compression occurring in different directions at different times throughout the orbit. These timing and amplitude of the peak stress experienced at each feature location varies with the feature's position on the moon (Figure 7).

Because we are most interested in the peak stresses experienced by these features—peak extension for paterae, peak compression for mountains—we calculate the maximum σ_1 value (using the convention where tension is positive) experienced by each patera, and the corresponding orientation on the surface of the stress vector, and the minimum σ_3 value and corresponding orientation experienced by each mountain. The average stress experienced at each feature, weighted by stress magnitude, was also calculated, but did not have any statistically significant relationship to feature orientation. We focus on maximum stress because the magnitude of these tidal stresses is one to two orders of magnitude smaller than the compressive breaking strength of basalt at ambient temperature on Earth (Cardarelli, 2018), so the maximum stress is necessary to come close to influencing fault movement. Of course, uniquely Ionian processes affecting the strength of the crust, such as sulfur dioxide frost interbeds, crystal size, temperature gradients, and lava flow morphology all influence (and possibly reduce) the breaking strength of the crust, bringing it closer to the range of modeled maximum stresses.

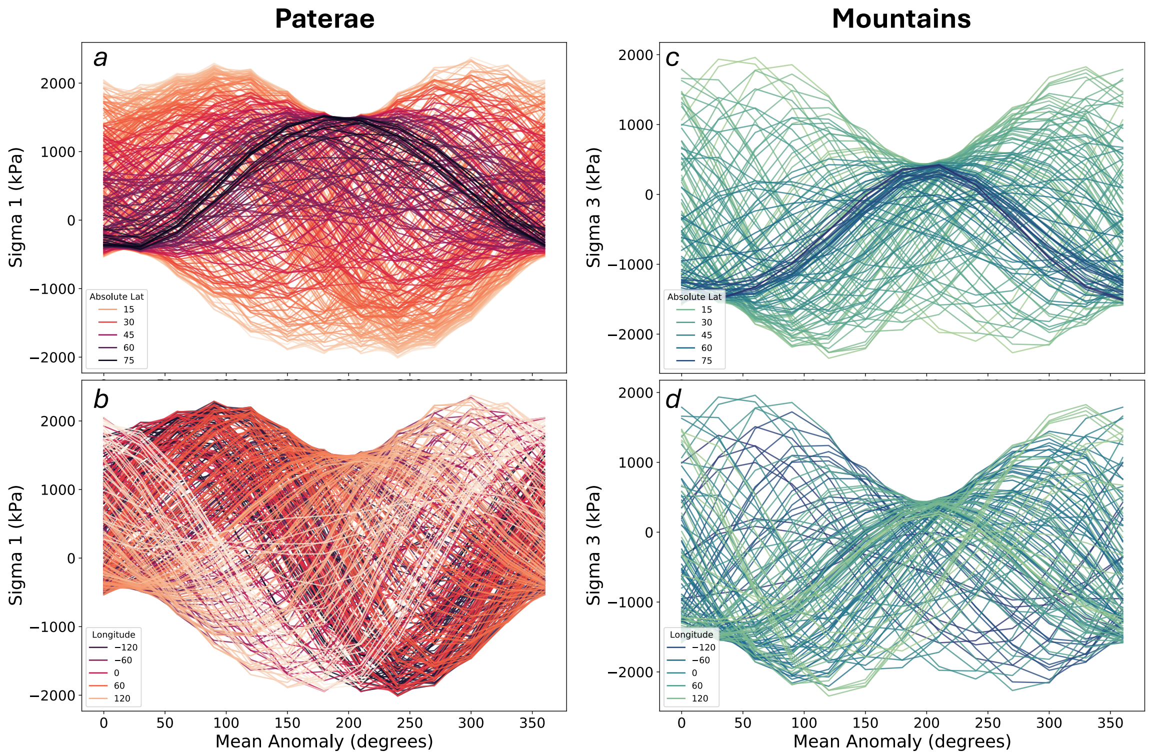

Figure 7. Model outputs from SatStressGUI for diurnal tidal stresses experienced at the location of each feature in the study throughout one orbit of Io around Jupiter (mean anomaly of zero corresponds to periapsis), at 30° increments. Stresses were modeled for σ_1 at all paterae (*a, b*) and σ_3 at all mountains (*c, d*). (*a*) and (*c*) show the change in timing of peak stress for features located near the equator (lighter colors) vs. the poles (darker colors), plotted as absolute value of latitude. (*b*) and (*d*) show the change in timing of peak stress for features at different longitudes around the moon, from the subjovian point at 0° (darker colors) around 360° to the east (lighter colors).

4.2 Correlations between stresses and features

We consider whether tidal stresses may influence the formation of the populations of elongate paterae that have a measurable orientation on the surface. For each location on Io's surface with one of these features, we extract the orientation and magnitude of the modeled maximum compressive and tensile stress experienced during one orbit of Jupiter at that location. The difference between the feature orientation and the maximum stress orientation guides our study: compressive stresses in one direction may produce uplifted mountains perpendicular to stress, and extension in one direction may result in elongate paterae perpendicular to stress as the crust opens like a fissure. We therefore calculate the difference between each feature orientation and the orientation of the maximum stress it experiences, and mirror these differences across the x-axis to better assess the parallel vs. perpendicular cases (Figure 8). That is, a feature oriented 100° from the orientation of maximum stress is the same as being oriented 80° from said stress vector, as both are 10° from perpendicular.

We present the overall relationships between all elongate (aspect ratio <0.72) paterae and mountains and their corollary maximum stress vectors in Figure 8, but calculated similar distributions for all the regions outlined in Figure 4 and Figure 6. Polar histograms of the difference between the two orientations are displayed in a single quadrant to highlight parallel and perpendicular relationships, but the Kuiper test for uniformity was performed on the differences as measured 0-180° (Table 2).

The differences between paterae and stress direction do not have a non-uniform distribution indicating a preferential orientation (*p*-value of 0.0583). The patera orientation distribution may be multimodal, which is why the first-order Kuiper test fails to find a significant result in the orientations; visual inspection of the rose plots suggests there may be peaks at ~0° and 90°. The Kuiper test also fails to detect any significant non-uniformity in the regional subsets analyzed in Figure 4. The subjovian hemisphere paterae, which demonstrated a strong preference away from NE/SW orientations, does not demonstrate a significant preferential offset from stress orientation (*p*-value = 0.0242).

Similarly, the mountain dataset does not exhibit a correlation between feature orientation and stress direction (*p*-value = 0.1354), though there are larger populations of mountains oriented 0-30° and 60° from peak stress orientation than other angles. The northern hemisphere, which has a significant preferential N-S orientation, also has a significant preferential offset from stress (*p*-value = 0.0068) with mountains most likely to be within 30° of parallel to stress. The south polar region exhibits a weaker but significant offset as well (*p*-value = 0.0095), with the most likely offsets being 25°or 60°, but caution should be exercised in interpreting this relationship due to the very small number of features in this region (N=14).

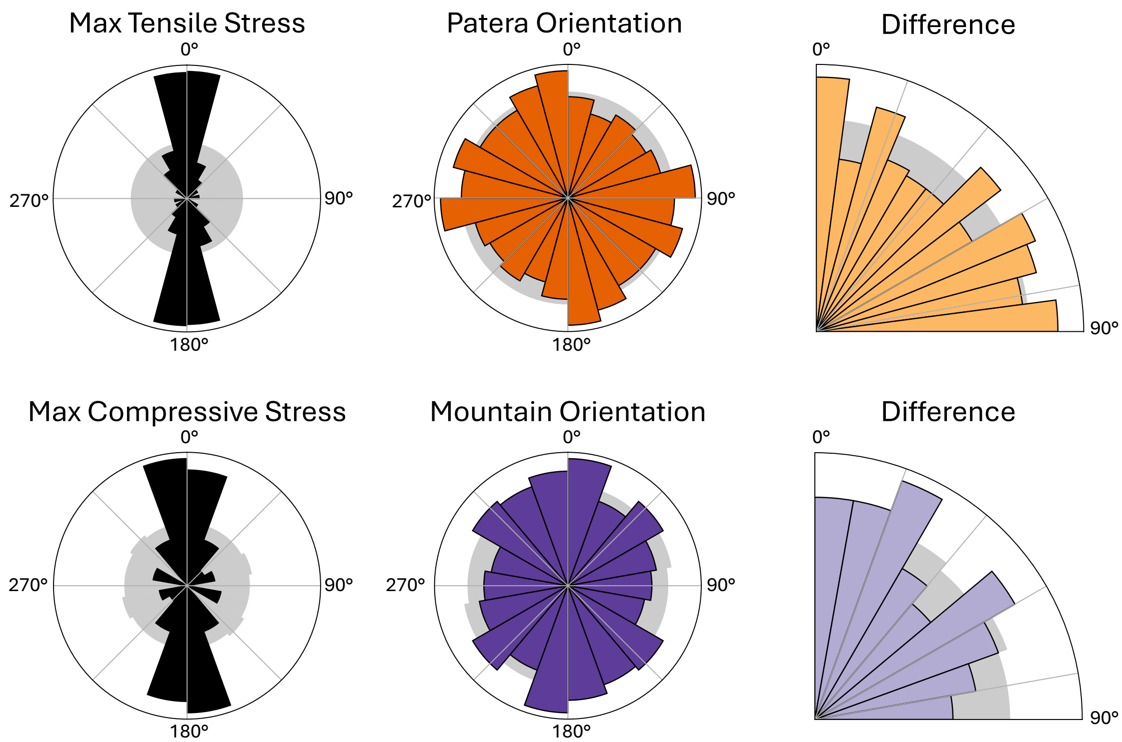

Figure 8. Orientations of elongate paterae (N=242), mountains (N=93), modeled maximum diurnal tidal stresses experienced at each feature location, and the difference between them for each feature. All orientations are measured in degrees east from north, and gray regions represent a uniform distribution for each dataset. Differences greater than 90 are reflected up over the x-axis to better visualize features parallel vs. perpendicular to stresses.

5. Discussion

5.1 Patera Stress Relationships

While the mechanisms surrounding tidal influence on mountain and patera formation are unclear, the spatial relationships between these features and the modeled stress field are important. We did not find any regions where there is a significant preferential orientation of features perpendicular to peak stress with an intuitive relation to the stress field.

Paterae are surface features deeply connected to the movement of magma upward and outward across Io's plains. They are much deeper than volcanic calderas on Earth, with walls that can exceed the Grand Canyon in depth (Radebaugh et al., 2001; White & Schenk, 2015). There are several models for the movement of magma to the surface to express as paterae, including using faulted crust as a pathway to the surface, or upwelling and melting through sulfur dioxide frost layers (Davies et al., 2006; Jaeger et al., 2003; Keszthelyi et al., 2004; 2007; Kirchoff & McKinnon, 2009; McKinnon et al., 2001; O'Reilly & Davies, 1981; Spencer et al., 2020). In either model, it is not unreasonable to predict that periodic flexing of the crust in diurnal cycles could influence the opening of fissures on the surface, perpendicular to those extensional stresses. Therefore, paterae might be expected to be better indicators of a feature-tidal stress relationship than mountains, which are thought to be generated by deep compressive crustal subsidence stresses, orders of magnitude larger than tides. The global ~uniform distribution of patera orientations and offsets from stress orientations indicates that there is no imprint of tidal stresses on the shape of paterae on the surface. However, it should be noted if these features initiate as narrow rifts, it is possible any initial shape is quickly modified by subsequent eruptive activity, new lava flows, and sapping of crater walls producing scalloped cliffsides (Moore et al., 2002). Though tidal stresses may not control the global population of patera orientations, they could still contribute to initial rifting and regional orientation trends.

For example, the strong preferential orientation of paterae in the subjovian hemisphere is striking, with a scarcity of features forming in a NE-SW orientation (Figure 4). Further subdividing this group of paterae to only include those in both the subjovian and leading hemispheres, thus encompassing one of the two antipodal clusters of paterae on Io (Kirchoff et al., 2011), yields a similar result (significantly nonuniform distribution with very few paterae oriented NE-SW; p-value = 0.0161, N=72). While the differenced distributions do not have a significantly nonuniform distribution according to the Kuiper test, they both show a large population of features oriented parallel and perpendicular to stresses. Though the subjovian hemisphere does contain a lower density of hot spots and lower heat flow, it also includes the massive and active Loki Patera, proposed to be linked to a crustal hot spot of mantle upwelling (Davies et al., 2015; Steinke et al., 2020). It is possible that the volcanic plumbing supporting this eruptive center disrupts the regional magma pathways, preventing proximal paterae from forming with the NE-SW orientation. On a longer timescale, it is possible that crustal formation from Loki-centric lava flows contributes to local heterogeneities that then manifest in preferential rifting orientations. Ultimately, factors beyond tidal stresses must be preventing paterae from forming or remaining oriented in a NE-SW direction in the subjovian hemisphere.

5.2 Mountain Stress Relationships

Because mountain formation is hypothesized to be driven by crustal subsidence stresses—which are orders of magnitude stronger than the surface tidal stresses—we do not expect tidal stresses to be strongly influential on the mountain uplift (e.g., McEwen et al., 2004; McKinnon et al., 2001; Schenk & Bulmer 1998). Therefore, it is not surprising that the mountains globally do not have a statistical correlation with tidal stresses orientations (Figure 8). However, the preferential N-S orientation of the mountains in the northern hemisphere, as well as their tendency to form parallel to direction of maximum compression, hints that there could be some contribution from stresses to slip along faults, but more but more detailed modeling of the stress components, particularly shear, may be useful to further illuminate this relationship in future work. It is possible cyclical compression could drive incremental motion along mountain-bounding faults with a directional bias.

Perhaps more than paterae, mountains are strongly impacted by erosional processes on Io, with their dramatic scarps being softened by processes of mass wasting and erosion over geologic time on a body constantly being shaken by volcanically-induced seismicity (e.g., Moore et al., 2002; Schenk & Bulmer, 1998; Seeger et al., 2025). These erosional processes could obscure any characteristic shape a mountain has when it is freshly uplifted, softening the features and making them rounder over time. Higher resolution global coverage of Io's mountains would allow us to better distinguish scarp from slump components of individual mountains, providing a better metric to understand the distribution of orientations (Figure 5). Mountain identification is also highly dependent on solar incidence angle. Though there is some variation in incidence angle between the northern and southern hemisphere by *Galileo*, it does not appear dramatic enough to strongly skew the N-S orientation bias of the northern hemisphere mountains compared to the southern hemisphere (Figure 7 in Williams et al., 2011).

6. Conclusions

Io’s diverse surface features include towering tectonic mountain massifs and depressed volcanic paterae that are diverse in size, shape, and spatial distribution. Hypothesized mountain formation mechanisms are driven by crustal subsidence stresses, which are orders of magnitude stronger than the tidal stresses that act on Io’s surface, while subsurface pathways bringing magma to the surface at eruptive paterae may be more susceptible to the flexing of the crust in different orientations and to different degrees throughout Io’s orbit. Because tidal stresses have been shown to affect surface feature formation elsewhere in the solar system, we modeled the tidal stresses acting on Io’s surface at the locations of all elongate mountains and paterae (meaning those with an aspect ratio <0.72) to determine if tidal stresses may influence surface feature formation by affecting their shape and map-view orientation. Both compressive and extensional maximum stresses have a preferential north-south orientation. Paterae tend to be more circular in shape than mountain blocks, but those that are elongate do have a characteristic planform aspect ratio of 2:3. Globally, the orientations of both mountains and paterae cannot be shown to be non-uniform according to the Kuiper test of uniformity. Moreover, there is no significant non-uniformity their offset from the direction of maximum tensile stress (for paterae) and compressive stress (for mountains) that they experience during Io’s orbit. A significant lack of paterae oriented NE-SW in the subjovian hemisphere, where Loki Patera is located, hints that there may be more complicated stresses influencing the regime, especially if Loki is a site of mantle upwelling. Mountains in the northern hemisphere show a significant trend of N-S alignment. Ultimately, though the distributions of measurements and modeled stresses do not support the hypothesized perpendicular relationships indicative of tidal stress influence on feature formation, this study reveals regional asymmetries in feature orientation and hints at relationships between feature orientation and stress that are likely compounded by crustal heterogeneities at depth influencing both tectonic uplift and magma pathways.

Acknowledgements

We thank thesis committee members Mike Lamb, John Grotzinger, and Bethany Ehlmann for their thorough comments and helpful discission about material properties on Io that helped in framing this work. Funding for this paper was provided by the NASA ROSES Solar System Workings program (through Task Order 80NM0018F0612).

Data Availability Statement

USGS geologic map shapefiles and *Voyager/Galileo* basemap are archived and freely available to the public via the Arizona State University Ronald Greeley Center for Planetary Studies (https://rgcps.asu.edu/gis_data/; Williams et al., 2021). SatStressGUI is a free and open-source program developed at NASA's Jet Propulsion Laboratory and is available for download from GitHub (https://github.com/SatStressGUI). All measured patera and mountain orientations and stress orientations can be found in Supplementary Data Tables S1 and S2.

References

Ahern, A. A., Radebaugh, J., Christiansen, E. H., Harris, R. A., & Tass, E. S. (2017). Lineations and structural mapping of Io's paterae and mountains: Implications for internal stresses. *Icarus*, *297*, 14-32. https://doi.org/10.1016/j.icarus.2017.06.004

Anderson, E. M. (1905). The dynamics of faulting. *Transactions of the Edinburgh Geological Society*, *8*(3), 387-402. https://doi.org/10.1144/transed.8.3.387

Aygün, B., & Čadek, O. (2025). Love numbers for Io with a magma ocean. *Icarus*, 116567. https://doi.org/10.1016/j.icarus.2025.116567

Baas, J. H. (2000). EZ-ROSE: a computer program for equal-area circular histograms and statistical analysis of two-dimensional vectorial data. *Computers & Geosciences*, *26*(2), 153-166. https://doi.org/10.1016/S0098-3004(99)00072-2

Baland, R. M., Yseboodt, M., & Van Hoolst, T. (2012). Obliquity of the Galilean satellites: The influence of a global internal liquid layer. *Icarus*, *220*(2), 435-448. https://doi.org/10.1016/j.icarus.2012.05.020

Bart, G. D., Turtle, E. P., Jaeger, W. L., Keszthelyi, L. P., & Greenberg, R. (2004). Ridges and tidal stress on Io. *Icarus*, *169*(1), 111-126. https://doi.org/10.1016/j.icarus.2004.01.003

Běhounková, M., Tobie, G., Čadek, O., Choblet, G., Porco, C., & Nimmo, F. (2015). Timing of water plume eruptions on Enceladus explained by interior viscosity structure. *Nature Geoscience*, *8*(8), 601-604. https://doi.org/10.1038/ngeo2475

Beuthe, M. (2015). Tides on Europa: The membrane paradigm. *Icarus*, *248*, 109-134. https://doi.org/10.1016/j.icarus.2014.10.027

Bunte, M. K., Williams, D. A., Greeley, R., & Jaeger, W. L. (2010). Geologic mapping of the Hi'iaka and Shamshu regions of Io. *Icarus*, *207*(2), 868-886. doi:10.1016/j.icarus.2009.12.006

Cardarelli, F. (2018). Rocks and Minerals. *Materials Handbook: A Concise Desktop Reference*, 883-1012. https://doi.org/10.1007/978-3-319-38925-7

Carr, M. H., McEwen, A. S., Howard, K. A., Chuang, F. C., Thomas, P., Schuster, P., ... & *Galileo* Imaging Team. (1998). Mountains and calderas on Io: Possible implications for lithosphere structure and magma generation. *Icarus*, 135(1), 146-165. Reclassified geologic units based on JunoCam imagery. https://doi.org/10.1006/icar.1998.5979

Cheng, H. C. J., & Klimczak, C. (2025). Tectonic patterns on Vesta and Ceres revealed by polygonal impact craters. *Icarus*, *433*, 116528. https://doi.org/10.1016/j.icarus.2025.116528

Davies, A. G., Keszthelyi, L. P., & Harris, A. J. (2010). The thermal signature of volcanic eruptions on Io and Earth. *Journal of Volcanology and Geothermal Research*, *194*(4), 75-99. https://doi.org/10.1016/j.jvolgeores.2010.04.009

Davies, A. G., Keszthelyi, L. P., Williams, D. A., Phillips, C. B., McEwen, A. S., Lopes, R. M., ... & Carlson, R. W. (2001). Thermal signature, eruption style, and eruption evolution at Pele and Pillan on Io. *Journal of Geophysical Research: Planets*, *106*(E12), 33079-33103. https://doi.org/10.1029/2000JE001357

Davies, A. G., Perry, J. E., Williams, D. A., Veeder, G. J., & Nelson, D. M. (2024). New global map of Io's volcanic thermal emission and discovery of hemispherical dichotomies. *The Planetary Science Journal*, *5*(5), 121. https://doi.org/10.3847/PSJ/ad4346

Davies, A. G., Veeder, G. J., Matson, D. L., & Johnson, T. V. (2015). Map of Io's volcanic heat flow. *Icarus*, *262*, 67-78. https://doi.org/10.1016/j.icarus.2015.08.003

Davies, A. G., Wilson, L., Matson, D., Leone, G., Keszthelyi, L., & Jaeger, W. (2006). The heartbeat of the volcano: The discovery of episodic activity at Prometheus on Io. *Icarus*, *184*(2), 460-477. doi:10.1016/j.icarus.2006.05.012

de Kleer, K., Nimmo, F., & Kite, E. (2019). Variability in Io's volcanism on timescales of periodic orbital changes. *Geophysical Research Letters*, *46*(12), 6327-6332. https://doi.org/10.1029/2019GL082691

Geissler, P., McEwen, A., Phillips, C., Keszthelyi, L., & Spencer, J. (2004). Surface changes on Io during the *Galileo* mission. *Icarus*, *169*(1), 29-64. https://doi.org/10.1016/j.icarus.2003.09.024

Girona, T., Huber, C., & Caudron, C. (2018). Sensitivity to lunar cycles prior to the 2007 eruption of Ruapehu volcano. *Scientific Reports*, *8*(1), 1476. https://doi.org/10.1038/s41598-018-19307-z

Greenberg, R. (1982). Orbital evolution of the Galilean satellites. *Satellites of Jupiter*, 65-92.

Groenleer, J. M., & Kattenhorn, S. A. (2008). Cycloid crack sequences on Europa: Relationship to stress history and constraints on growth mechanics based on cusp angles. *Icarus*, *193*(1), 158-181. https://doi.org/10.1016/j.icarus.2007.08.032

Hamilton, C. W., Beggan, C. D., Still, S., Beuthe, M., Lopes, R. M., Williams, D. A., ... & Wright, W. (2013). Spatial distribution of volcanoes on Io: Implications for tidal heating and magma ascent. *Earth and Planetary Science Letters*, *361*, 272-286. https://doi.org/10.1016/j.epsl.2012.10.032

Hedman, M. M., Gosmeyer, C. M., Nicholson, P. D., Sotin, C., Brown, R. H., Clark, R. N., ... & Showalter, M. R. (2013). An observed correlation between plume activity and tidal stresses on Enceladus. *Nature*, *500*(7461), 182-184. https://doi.org/10.1038/nature12371

Hunter, J. D. (2007). Matplotlib: A 2D graphics environment. *Computing in Science & Engineering*, *9*(03), 90-95. DOI: 10.1109/MCSE.2007.55

Hurford, T. A., Helfenstein, P., Hoppa, G. V., Greenberg, R., & Bills, B. G. (2007). Eruptions arising from tidally controlled periodic openings of rifts on Enceladus. *Nature*, *447*(7142), 292-294. https://doi.org/10.1038/nature05821

Jaeger, W. L., Turtle, E. P., Keszthelyi, L. P., Radebaugh, J., McEwen, A. S., & Pappalardo, R. T. (2003). Orogenic tectonism on Io. *Journal of Geophysical Research: Planets*, *108*(E8). https://doi.org/10.1029/2002JE001946

Jammalamadaka, S. R., & Sengupta, A. (2001). *Topics in circular statistics* (Vol. 5). World Scientific.

Jara-Orué, H. M., & Vermeersen, B. L. (2011). Effects of low-viscous layers and a non-zero obliquity on surface stresses induced by diurnal tides and non-synchronous rotation: The case of Europa. *Icarus*, *215*(1), 417-438. https://doi.org/10.1016/j.icarus.2011.05.034

Johnson, T. V., Cooke, I. I., Sagan, C., & Soderblom, L. A. (1979). Volcanic resurfacing rates and implications for volatiles on Io. *Nature (London);(United Kingdom)*, *280*(5725). https://doi.org/10.1038/280746a0

Keszthelyi, L., Jaeger, W., Milazzo, M., Radebaugh, J., Davies, A. G., & Mitchell, K. L. (2007). New estimates for Io eruption temperatures: Implications for the interior. *Icarus*, *192*(2), 491-502. https://doi.org/10.1016/j.icarus.2007.07.008

Keszthelyi, L., Jaeger, W. L., Turtle, E. P., Milazzo, M., & Radebaugh, J. (2004). A post-*Galileo* view of Io's interior. *Icarus*, *169*(1), 271-286. https://doi.org/10.1016/j.icarus.2004.01.005

Khurana, K. K., Jia, X., Kivelson, M. G., Nimmo, F., Schubert, G., & Russell, C. T. (2011). Evidence of a global magma ocean in Io's interior. *Science*, *332*(6034), 1186-1189. DOI: 10.1126/science.1201425

Kirchoff, M. R., & McKinnon, W. B. (2009). Formation of mountains on Io: Variable volcanism and thermal stresses. *Icarus*, *201*(2), 598-614. https://doi.org/10.1016/j.icarus.2009.02.006

Kirchoff, M. R., McKinnon, W. B., & Schenk, P. M. (2011). Global distribution of volcanic centers and mountains on Io: Control by asthenospheric heating and implications for mountain formation. *Earth and Planetary Science Letters*, *301*(1-2), 22-30. https://doi.org/10.1016/j.epsl.2010.11.018

Klimczak, C., Crane, K. T., & Byrne, P. K. (2025). Mercury has multiple, superposed global tectonic patterns. *Earth and Planetary Science Letters*, *658*, 119331. https://doi.org/10.1016/j.epsl.2025.119331

Kneissl, T., van Gasselt, S., & Neukum, G. (2011). Map-projection-independent crater size-frequency determination in GIS environments—New software tool for ArcGIS. *Planetary and Space Science*, *59*(11-12), 1243-1254. https://doi.org/10.1016/j.pss.2010.03.015

Kuiper, N. H. (1960, January). Tests concerning random points on a circle. In *Nederlandse Akademie van Wetenschappen Proceedings Series A*, 63(1), 38-47.

Lainey, V., Duriez, L., & Vienne, A. (2006). Synthetic representation of the Galilean satellites orbital motions from L1 ephemerides. *Astronomy & Astrophysics*, **456**, 783–788. https://doi.org/10.1051/0004-6361:20064941

Landler, L., Ruxton, G. D., & Malkemper, E. P. (2018). Circular data in biology: advice for effectively implementing statistical procedures. *Behavioral Ecology and Sociobiology*, *72*, 1-10. https://doi.org/10.1007/s00265-018-2538-y

Lopes, R. M., Kamp, L. W., Douté, S., Smythe, W. D., Carlson, R. W., McEwen, A. S., ... & Soderblom, L. A. (2001). Io in the near infrared: Near-Infrared Mapping Spectrometer (NIMS) results from the *Galileo* flybys in 1999 and 2000. *Journal of Geophysical Research: Planets*, *106*(E12), 33053-33078. https://doi.org/10.1029/2000JE001463

McEwen, A. S., Keszthelyi, L., Geissler, P., Simonelli, D. P., Carr, M. H., Johnson, T. V., ... & Schubert, G. (1998). Active volcanism on Io as seen by *Galileo* SSI. *Icarus*, *135*(1), 181-219. https://doi.org/10.1006/icar.1998.5972

McEwen, A. S., Keszthelyi, L. P., Lopes, R., Schenk, P. M., & Spencer, J. R. (2004). The lithosphere and surface of Io. *Jupiter: The Planet, Satellites and Magnetosphere*, 1, 307-328.

McKinnon, W. B., Schenk, P. M., & Dombard, A. J. (2001). Chaos on Io: A model for formation of mountain blocks by crustal heating, melting, and tilting. *Geology*, *29*(2), 103-106. https://doi.org/10.1130/0091-7613(2001)029<0103:COIAMF>2.0.CO;2

Moore, J. M., Sullivan, R. J., Chuang, F. C., Head III, J. W., McEwen, A. S., Milazzo, M. P., ... & Turtle, E. P. (2001). Landform degradation and slope processes on Io: The *Galileo* view. *Journal of Geophysical Research: Planets*, *106*(E12), 33223-33240. https://doi.org/10.1029/2000JE001375

Olgin, J. G., Smith-Konter, B. R., & Pappalardo, R. T. (2011). Limits of Enceladus's ice shell thickness from tidally driven tiger stripe shear failure. *Geophysical Research Letters*, *38*(2), L02201. https://doi.org/10.1029/2010GL044950

O'Reilly, T. C., & Davies, G. F. (1981). Magma transport of heat on Io: A mechanism allowing a thick lithosphere. *Geophysical Research Letters*, *8*(4), 313-316. https://doi.org/10.1029/GL008i004p00313

Park, R. S., Jacobson, R. A., Gomez Casajus, L., Nimmo, F., Ermakov, A. I., Keane, J. T., ... & Bolton, S. J. (2025). Io's tidal response precludes a shallow magma ocean. *Nature*, *638*(8049), 69-73. https://doi.org/10.1038/s41586-024-08442-5

Patthoff, D. A., & Davies, A. G. (2017). Tidal Stresses and Volcanism on Io. In *48th Annual Lunar and Planetary Science Conference* (No. 1964, p. 1748).

Peale, S. J., Cassen, P., & Reynolds, R. T. (1979). Melting of Io by tidal dissipation. *Science*, *203*(4383), 892-894. DOI: 10.1126/science.203.4383.892

Perry, J. E., Davies, A. G., Williams, D. A., & Nelson, D. M. (2025). Hot Spot Detections and Volcanic Changes on Io during the Juno Epoch: Orbits PJ5 to PJ55. *The Planetary Science Journal*, *6*(4), 84. https://doi.org/10.3847/PSJ/adbae3

Price-Whelan, Adrian M., Pey Lian Lim, Nicholas Earl, Nathaniel Starkman, Larry Bradley, David L. Shupe, Aarya A. Patil et al. "The Astropy Project: sustaining and growing a community-oriented open-source project and the latest major release (v5. 0) of the core package." *The Astrophysical Journal* 935, no. 2 (2022): 167. DOI: 10.3847/1538-4357/ac7c74

Radebaugh, J., Keszthelyi, L. P., McEwen, A. S., Turtle, E. P., Jaeger, W., & Milazzo, M. (2001). Paterae on Io: A new type of volcanic caldera? *Journal of Geophysical Research: Planets*, *106*(E12), 33005-33020. https://doi.org/10.1029/2000JE001406

Rhoden, A. R., Henning, W., Hurford, T. A., Patthoff, D. A., & Tajeddine, R. (2017). The implications of tides on the Mimas ocean hypothesis. *Journal of Geophysical Research: Planets*, *122*(2), 400-410. https://doi.org/10.1002/2016JE005097

Rhoden, A. R., Hurford, T. A., Roth, L., & Retherford, K. (2015). Linking Europa's plume activity to tides, tectonics, and liquid water. *Icarus*, *253*, 169-178. https://doi.org/10.1016/j.icarus.2015.02.023

Ross, M. N., & Schubert, G. (1985). Tidally forced viscous heating in a partially molten Io. *Icarus*, *64*(3), 391-400. https://doi.org/10.1016/0019-1035(85)90063-6

Ross, M. N., Schubert, G., Spohn, T., & Gaskell, R. W. (1990). Internal structure of Io and the global distribution of its topography. *Icarus*, *85*(2), 309-325. https://doi.org/10.1016/0019-1035(90)90119-T

Sanderson, D. J., & Peacock, D. C. (2020). Making rose diagrams fit-for-purpose. *Earth-Science Reviews*, *201*, 103055. https://doi.org/10.1016/j.earscirev.2019.103055

Schenk, P. M., & Bulmer, M. H. (1998). Origin of mountains on Io by thrust faulting and large-scale mass movements. *Science*, *279*(5356), 1514-1517. DOI: 10.1126/science.279.5356.1514

Schenk, P., Hargitai, H., Wilson, R., McEwen, A., & Thomas, P. (2001). The mountains of Io: Global and geological perspectives from *Voyager* and *Galileo*. *Journal of Geophysical Research: Planets*, *106*(E12), 33201-33222. https://doi.org/10.1029/2000JE001408

Scott, D. W. (1979). On optimal and data-based histograms. *Biometrika*, *66*(3), 605-610. https://doi.org/10.1093/biomet/66.3.605

Seeger, C., de Kleer, K., Williams, D., Perry, J., Davies, A., & Nelson, D. M. (2024). Insights Into Surface Evolution on io Based on Junocam PJ57 and PJ58 Flybys. In *Geological Society of America Abstracts* (Vol. 56, p. 405067).

Segatz, M., Spohn, T., Ross, M. N., & Schubert, G. (1988). Tidal dissipation, surface heat flow, and figure of viscoelastic models of Io. *Icarus*, *75*(2), 187-206. https://doi.org/10.1016/0019-1035(88)90001-2

Smith-Konter, B., & Pappalardo, R. T. (2008). Tidally driven stress accumulation and shear failure of Enceladus's tiger stripes. *Icarus*, *198*(2), 435-451. https://doi.org/10.1016/j.icarus.2008.07.005

Sottili, G., & Palladino, D. M. (2012). Tidal modulation of eruptive activity at open-vent volcanoes: evidence from Stromboli, Italy. *Terra Nova*, *24*(3), 233-237. https://doi.org/10.1111/j.1365-3121.2012.01059.x

Spencer, D. C., Katz, R. F., & Hewitt, I. J. (2020). Magmatic intrusions control Io's crustal thickness. *Journal of Geophysical Research: Planets*, *125*(6), e2020JE006443. https://doi.org/10.1029/2020JE006443

Steinke, T., van Sliedregt, D., Vilella, K., Van der Wal, W., & Vermeersen, B. (2020). Can a combination of convective and magmatic heat transport in the mantle explain Io's volcanic pattern? *Journal of Geophysical Research: Planets*, *125*(12), e2020JE006521. https://doi.org/10.1029/2020JE006521

Tackley, P. J., Schubert, G., Glatzmaier, G. A., Schenk, P., Ratcliff, J. T., & Matas, J. P. (2001). Three-dimensional simulations of mantle convection in Io. *Icarus*, *149*(1), 79-93. https://doi.org/10.1006/icar.2000.6536

Turtle, E. P., Jaeger, W. L., Keszthelyi, L. P., McEwen, A. S., Milazzo, M., Moore, J., ... & Schuster, P. (2001). Mountains on Io: High-resolution *Galileo* observations, initial interpretations, and formation models. *Journal of Geophysical Research: Planets*, *106*(E12), 33175-33199. https://doi.org/10.1029/2000JE001354

Veeder, G. J., Davies, A. G., Matson, D. L., Johnson, T. V., Williams, D. A., & Radebaugh, J. (2012). Io: Volcanic thermal sources and global heat flow. *Icarus*, *219*(2), 701-722. https://doi.org/10.1016/j.icarus.2012.04.004

Veeder, G. J., Matson, D. L., Johnson, T. V., Blaney, D. L., & Goguen, J. D. (1994). Io's heat flow from infrared radiometry: 1983–1993. *Journal of Geophysical Research: Planets*, *99*(E8), 17095-17162. https://doi.org/10.1029/94JE00637

Wahr, J., Selvans, Z. A., Mullen, M. E., Barr, A. C., Collins, G. C., Selvans, M. M., & Pappalardo, R. T. (2009). Modeling stresses on satellites due to nonsynchronous rotation and orbital eccentricity using gravitational potential theory. *Icarus*, *200*(1), 188-206. https://doi.org/10.1016/j.icarus.2008.11.002

White, O. L., & Schenk, P. M. (2015). Topographic mapping of paterae and layered plains on Io using photoclinometry. *Journal of Geophysical Research: Planets*, *120*(1), 51-61. https://doi.org/10.1002/2014JE004672

Williams, D. A., Keszthelyi, L. P., Crown, D. A., Yff, J. A., Jaeger, W. L., Schenk, P. M., ... & Becker, T. L. (2011). *Geologic Map of Io*. US Department of the Interior, US Geological Survey.

Williams, D. A., Keszthelyi, L. P., Crown, D. A., Yff, J. A., Jaeger, W. L., Schenk, P. M., ... & Becker, T. L. (2011). Volcanism on Io: New insights from global geologic mapping. *Icarus*, *214*(1), 91-112. https://doi.org/10.1016/j.icarus.2011.05.007

Williams, D. A., Nelson, D. M., & Milazzo, M. P. (2021). The Io GIS Database 1.0: a proto-Io planetary spatial data infrastructure. *The Planetary Science Journal*, *2*(4), 148. https://doi.org/10.3847/PSJ/ac097f.

Supplementary Data for Chapter 2

This section contains all data used in evaluating surface feature shape, orientation, and relationship to diurnal tidal stresses. Table S1 (p. 47-55) contains data for elongate paterae (planform aspect ratios of <0.72). Table S2 (p. 56-59) contains data for all mountains, though the elongate population with aspect ratios of <0.72 was isolated for analysis in Chapter 2. In both tables, Latitude and Longitude (0-180, East positive) correspond to the midpoint of each patera or mountain polygon. Width and Length refer to the geodesic length (in km) of the long and short axis of a minimum bounding rectangle encasing each feature. Orientation is the orientation in degrees of the long axis of that rectangle measured clockwise from north. The absolute value of the difference between the stress orientation and feature orientation is given in both the original 0-180 measurement and as 0-90, where all values >90 are reflected back up over the x-axis as in Figure 8. For Mountains, Unit corresponds to geologic units in USGS geologic map (Williams et al., 2011); Ml = Mountain, lineated; Mm = Mountain, mottled; Mu = Mountain, undivided. Note that Object_ID refers to unique identifier in ArcPro map based on drawing order; table is sorted in order of increasing latitude so some Object_ID values are slightly out of chronological order.

Table S1. Measurements and modeled stress orientations for paterae.

Object_ID	Latitude	Longitude	Width	Length	Feature_ Orientation	Aspect_ ratio	Sigma1 _max_kPa	Stress_ orientation	Orientation_ Diff_0-180	Orientation_ Diff_0-90
1	-74.743737	134.397056	15.203	24.377	63.13	0.6236	1316.47	138.18	75.05	75.05
3	-73.583586	23.195217	37.752	68.047	27.50	0.5548	1243.12	48.34	20.84	20.84
4	-72.940382	-107.21956	65.476	91.963	6.55	0.7120	1416.46	179.77	173.22	6.78
7	-69.967242	64.655206	40.398	112.165	123.79	0.3602	1400.60	7.45	116.34	63.66
9	-68.80469	-109.73564	45.241	75.672	118.09	0.5979	1414.74	2.16	115.93	64.07
10	-68.381175	-155.18873	34.312	48.860	111.47	0.7022	1161.62	36.25	75.22	75.22
13	-65.111437	31.166622	59.248	92.836	157.40	0.6382	1172.47	29.55	127.85	52.15
14	-64.995269	-3.82907	66.190	120.972	12.91	0.5472	847.82	75.26	62.35	62.35
19	-62.676303	115.755281	63.226	113.026	161.16	0.5594	1361.21	169.74	8.58	8.58
24	-59.451267	-32.033322	59.894	83.396	80.08	0.7182	1123.23	153.79	73.71	73.71
22	-59.308225	169.87493	28.950	45.794	177.50	0.6322	766.31	136.03	41.47	41.47
21	-59.021649	93.49632	20.900	31.188	61.93	0.6701	1415.71	172.60	110.67	69.33
25	-58.642768	-169.09763	31.437	47.854	177.33	0.6569	821.99	41.36	135.97	44.03
29	-55.645046	108.933042	35.416	55.682	71.58	0.6360	1405.12	176.18	104.60	75.40
33	-54.258907	90.920482	13.857	34.159	16.51	0.4057	1417.68	175.09	158.58	21.42
31	-54.112972	108.966933	11.141	18.040	68.99	0.6176	1412.96	176.21	107.22	72.78
38	-53.251426	17.407847	84.913	168.851	12.26	0.5029	904.99	27.91	15.65	15.65
36	-52.246727	166.270166	48.250	71.697	77.30	0.6730	844.14	149.84	72.54	72.54
37	-51.899788	157.469691	33.175	50.438	30.54	0.6577	1024.18	155.64	125.10	54.90
39	-50.507046	-41.545175	14.961	32.706	175.63	0.4574	1341.41	167.28	8.35	8.35
40	-49.900522	-0.716172	30.746	45.233	25.17	0.6797	627.15	145.67	120.50	59.50
42	-49.767408	-48.17529	45.685	69.385	172.53	0.6584	1406.20	169.77	2.76	2.76
43	-49.7469	124.00889	56.533	88.495	67.56	0.6388	1433.28	172.82	105.26	74.74
41	-49.547661	165.670785	20.552	45.153	8.28	0.4552	900.82	150.54	142.26	37.74
45	-49.474448	30.156603	40.260	68.844	132.46	0.5848	1187.28	15.05	117.41	62.59
50	-49.019143	40.27841	43.315	91.513	1.91	0.4733	1340.83	8.59	6.68	6.68
49	-48.698798	-124.18151	64.972	102.549	113.85	0.6336	1464.42	178.07	64.22	64.22
47	-48.629039	94.248556	41.851	123.539	108.14	0.3388	1415.34	177.98	69.84	69.84

Object_ID	Latitude	Longitude	Width	Length	Feature_ Orientation	Aspect_ ratio	Sigma1 _max_kPa	Stress_ orientation	Orientation_ Diff_ 0-180	Orientation_ Diff_ 0-90
52	-48.370182	-11.805123	82.821	132.059	97.65	0.6271	886.63	150.78	53.13	53.13
53	-47.415529	-179.41282	22.878	40.068	84.65	0.5710	662.22	147.77	63.12	63.12
56	-47.334919	-108.78107	51.700	81.265	42.93	0.6362	1468.91	172.64	129.71	50.29
55	-46.943796	-81.752782	27.821	60.038	110.00	0.4634	1421.86	179.89	69.89	69.89
60	-44.81662	-41.070507	24.971	46.760	91.67	0.5340	1450.34	170.56	78.89	78.89
62	-43.327185	120.934763	21.634	33.007	58.64	0.6554	1532.48	179.31	120.67	59.33
64	-42.155958	-160.45636	12.286	23.815	158.97	0.5159	1139.68	16.01	142.96	37.04
65	-41.877142	152.372451	23.512	53.731	99.69	0.4376	1335.75	164.44	64.75	64.75
69	-41.68556	55.658001	70.481	102.657	106.38	0.6866	1551.23	178.18	71.80	71.80
67	-41.638313	-137.85812	14.260	34.091	65.67	0.4183	1502.88	3.50	62.17	62.17
70	-40.824666	34.432841	18.132	28.311	170.66	0.6405	1421.59	7.27	163.39	16.61
68	-40.779198	26.916964	10.819	16.856	77.68	0.6419	1302.32	11.47	66.21	66.21
73	-40.276802	20.889857	28.499	43.895	156.82	0.6492	1201.42	14.38	142.44	37.56
78	-38.990585	-101.48841	48.589	68.353	157.61	0.7109	1459.46	172.08	14.47	14.47
79	-38.517664	6.838945	31.743	65.906	119.70	0.4816	996.27	10.92	108.78	71.22
77	-38.397493	69.365775	18.801	34.343	129.61	0.5474	1527.49	171.03	41.42	41.42
80	-38.006371	105.874225	19.065	32.892	92.40	0.5796	1497.71	2.86	89.54	89.54
85	-36.185893	152.051821	42.029	62.227	170.64	0.6754	1495.98	168.17	2.47	2.47
86	-35.600388	160.312432	26.939	47.478	145.59	0.5674	1377.80	162.66	17.07	17.07
87	-35.049847	-119.8033	31.232	51.319	122.20	0.6086	1635.38	175.09	52.89	52.89
88	-34.411817	-100.91371	21.581	33.875	80.09	0.6371	1463.45	172.42	92.33	87.67
93	-34.106272	-129.59841	58.404	115.876	150.58	0.5040	1686.86	176.30	25.72	25.72
95	-33.005988	13.397893	28.763	58.980	4.59	0.4877	1276.46	9.52	4.93	4.93
97	-31.334034	15.154402	10.286	16.389	87.45	0.6276	1354.42	7.12	80.33	80.33
99	-31.237223	47.825827	11.811	22.060	96.26	0.5354	1734.51	178.32	82.06	82.06
103	-31.097981	21.895502	44.443	76.919	158.64	0.5778	1475.58	9.24	149.40	30.60
102	-30.548656	87.606684	24.682	79.239	77.27	0.3115	1413.80	175.15	97.88	82.12
112	-27.586688	-38.383889	26.756	42.259	123.99	0.6331	1854.80	175.39	51.40	51.40

Object_ID	Latitude	Longitude	Width	Length	Feature_ Orientation	Aspect_ ratio	Sigma1 _max_kPa	Stress_ orientation	Orientation_ Diff_0-180	Orientation_ Diff_0-90
113	-27.40153	28.783739	24.626	43.332	104.29	0.5683	1679.14	5.38	98.91	81.09
114	-26.616174	17.962972	19.461	34.541	72.54	0.5634	1535.86	9.43	63.11	63.11
120	-26.390791	115.877293	64.712	96.936	10.56	0.6676	1737.40	2.38	8.18	8.18
122	-26.237395	-158.09372	74.284	126.174	147.42	0.5887	1616.39	4.46	142.96	37.04
121	-25.533518	102.709966	42.206	63.603	111.40	0.6636	1525.56	0.80	110.60	69.40
128	-24.204656	-16.666418	81.341	117.099	157.70	0.6946	1657.91	163.10	5.40	5.40
126	-24.113395	9.242514	38.763	95.610	42.79	0.4054	1492.85	177.50	134.71	45.29
124	-24.03618	-148.46072	19.296	49.736	168.81	0.3880	1806.04	2.72	166.09	13.91
129	-23.394752	-111.67098	53.551	92.086	157.70	0.5815	1649.81	174.47	16.77	16.77
135	-20.91544	-34.882224	13.668	40.424	91.58	0.3381	1978.83	175.87	84.29	84.29
139	-20.847258	173.368011	28.682	47.993	178.87	0.5976	1608.37	160.86	18.01	18.01
138	-20.684769	154.383613	17.595	40.889	177.10	0.4303	1876.46	170.98	6.12	6.12
140	-20.416133	27.384084	26.535	38.887	4.85	0.6824	1829.96	2.51	2.34	2.34
136	-20.366992	48.228111	8.847	15.062	145.73	0.5874	1931.34	175.68	29.95	29.95
137	-20.358723	35.282361	14.271	21.155	87.03	0.6746	1910.94	178.97	91.94	88.06
141	-19.875877	-160.10602	12.364	29.021	39.35	0.4261	1741.29	6.81	32.54	32.54
142	-19.354329	-82.839184	22.397	39.796	98.60	0.5628	1466.40	0.29	98.31	81.69
143	-19.138054	-2.570692	15.643	27.779	91.53	0.5631	1618.49	159.50	67.97	67.97
147	-18.744617	166.673126	34.870	53.134	175.48	0.6563	1734.38	163.04	12.44	12.44
148	-18.727629	-141.11149	53.275	76.263	108.70	0.6986	1968.34	179.72	71.02	71.02
146	-18.725256	103.816402	21.633	90.097	77.55	0.2401	1575.80	2.34	75.21	75.21
151	-18.687874	157.607356	25.788	93.287	170.86	0.2764	1871.16	170.93	0.07	0.07
153	-18.636734	-150.77126	47.216	112.238	164.01	0.4207	1893.93	0.87	163.14	16.86
150	-18.050878	-0.984925	30.230	47.614	177.84	0.6349	1637.46	155.24	22.60	22.60
154	-17.007716	-27.65534	18.847	33.376	148.28	0.5647	1985.34	173.36	25.08	25.08
152	-16.954711	-170.83566	3.865	6.230	106.26	0.6204	1675.95	177.11	70.85	70.85
157	-16.709487	44.761726	52.256	82.669	111.03	0.6321	1995.34	178.30	67.27	67.27
164	-16.456522	29.669598	58.132	182.800	49.29	0.3180	1933.85	0.11	49.18	49.18

Object_ID	Latitude	Longitude	Width	Length	Feature_ Orientation	Aspect_ ratio	Sigma1 _max_kPa	Stress_ orientation	Orientation_ Diff_ 0-180	Orientation_ Diff_ 0-90
160	-15.212564	-154.5489	5.729	8.820	22.04	0.6495	1906.66	179.96	157.92	22.08
162	-15.182156	62.073829	23.320	34.327	176.00	0.6794	1820.26	174.27	1.73	1.73
161	-14.975802	-32.533089	18.662	26.073	81.66	0.7158	2073.91	175.34	93.68	86.32
165	-14.584694	-167.93493	9.502	14.307	173.91	0.6642	1749.74	4.90	169.01	10.99
166	-14.428669	-1.168678	25.178	39.382	1.18	0.6393	1712.06	153.18	152.00	28.00
168	-13.961422	-21.9784	21.701	38.303	116.52	0.5666	1960.18	171.76	55.24	55.24
177	-13.505202	100.713398	54.772	153.536	42.82	0.3567	1531.73	0.96	41.86	41.86
171	-13.468745	-76.008433	14.162	21.422	175.99	0.6611	1599.00	1.52	174.47	5.53
170	-13.423188	-164.29844	6.743	14.637	13.67	0.4607	1808.74	6.40	7.27	7.27
176	-12.645568	-139.10587	19.593	34.493	96.13	0.5680	2063.58	178.79	82.66	82.66
175	-12.602892	63.22684	12.352	18.453	153.02	0.6694	1811.30	174.63	21.61	21.61
181	-11.548457	150.16401	28.196	39.609	38.13	0.7119	2090.71	176.59	138.46	41.54
186	-11.401202	-128.47856	32.057	57.699	58.51	0.5556	2011.27	176.11	117.60	62.40
185	-11.384235	-158.79322	30.734	88.488	83.15	0.3473	1911.96	3.97	79.18	79.18
188	-10.746304	-176.5578	17.278	42.851	160.65	0.4032	1763.74	144.91	15.74	15.74
196	-9.931846	22.433017	114.788	164.129	81.07	0.6994	1946.39	2.21	78.86	78.86
198	-9.883783	-63.566391	121.078	178.819	102.22	0.6771	1898.43	1.82	100.40	79.60
193	-9.366767	45.145176	61.851	146.331	91.04	0.4227	2077.85	176.93	85.89	85.89
203	-8.844525	134.422005	81.141	115.430	134.08	0.7029	2172.41	179.52	45.44	45.44
195	-8.817794	124.913989	22.529	34.851	162.53	0.6464	2074.66	0.98	161.55	18.45
197	-8.61489	35.189833	27.837	41.033	177.35	0.6784	2087.56	179.39	2.04	2.04
200	-8.54142	-158.01532	27.676	43.513	176.25	0.6360	1957.73	2.65	173.60	6.40
201	-8.347468	-43.975222	34.812	52.527	178.48	0.6627	2185.62	179.79	1.31	1.31
202	-8.253287	25.740339	35.547	59.942	29.72	0.5930	2003.17	179.46	149.74	30.26
199	-8.183727	-151.94615	15.274	30.575	110.17	0.4996	2034.73	1.22	108.95	71.05
208	-7.557891	-85.023217	77.183	128.745	48.14	0.5995	1445.99	0.39	47.75	47.75
207	-7.076856	47.205154	26.499	40.420	8.93	0.6556	2087.28	178.42	169.49	10.51
206	-6.701352	-175.77599	10.646	16.982	149.81	0.6269	1808.09	131.13	18.68	18.68

Object_ID	Latitude	Longitude	Width	Length	Feature_ Orientation	Aspect_ ratio	Sigma1 _max_kPa	Stress_ orientation	Orientation_ Diff_ 0-180	Orientation_ Diff_ 0-90
211	-6.599004	84.069302	64.448	98.109	172.76	0.6569	1431.06	178.44	5.68	5.68
212	-5.950212	169.564074	32.766	51.118	163.21	0.6410	1885.31	169.61	6.40	6.40
214	-5.944004	67.196645	54.926	79.442	90.21	0.6914	1754.37	177.54	87.33	87.33
217	-5.344217	48.17721	18.172	27.613	163.43	0.6581	2090.27	178.54	15.11	15.11
213	-5.312821	-132.03455	6.757	15.671	130.94	0.4312	2093.41	178.99	48.05	48.05
224	-5.165203	115.357576	83.997	148.688	54.76	0.5649	1892.96	0.68	54.08	54.08
219	-4.83283	-153.69094	4.457	9.238	53.31	0.4825	2036.82	179.75	126.44	53.56
220	-4.08711	129.894305	8.710	13.959	34.72	0.6239	2167.04	0.46	34.26	34.26
223	-3.837592	128.148987	9.902	24.834	130.89	0.3987	2141.01	0.17	130.72	49.28
228	-3.617658	-79.433182	76.246	138.018	111.09	0.5524	1541.50	0.19	110.90	69.10
227	-3.58507	154.765114	58.513	91.418	96.97	0.6401	2103.47	178.57	81.60	81.60
226	-3.477165	10.468605	36.860	55.802	112.57	0.6606	1862.54	173.38	60.81	60.81
230	-2.923509	56.312564	37.679	53.603	57.31	0.7029	1989.66	178.72	121.41	58.59
232	-1.65382	23.699168	10.231	14.724	83.91	0.6949	2023.12	0.04	83.87	83.87
236	-1.084843	142.639829	24.113	50.085	158.07	0.4814	2221.48	0.04	158.03	21.97
234	-0.970305	-144.76638	30.331	74.029	121.96	0.4097	2128.85	0.15	121.81	58.19
235	-0.658169	-152.40606	16.864	28.465	142.61	0.5924	2065.00	0.31	142.30	37.70
237	-0.471627	27.324652	22.478	56.100	118.99	0.4007	2060.91	179.89	60.90	60.90
238	0.121995	92.058595	24.552	42.091	69.84	0.5833	1421.41	0.01	69.83	69.83
240	0.371024	16.833039	23.753	56.994	44.84	0.4168	1935.49	179.62	134.78	45.22
243	0.549762	54.478272	83.047	146.243	55.85	0.5679	2023.54	179.96	124.11	55.89
253	1.058495	105.157518	126.649	186.266	50.31	0.6799	1644.52	179.98	129.67	50.33
247	1.212977	-167.61846	63.387	92.814	35.47	0.6829	1885.97	179.52	144.05	35.95
244	1.600511	166.749774	44.186	72.952	97.61	0.6057	1944.08	2.29	95.32	84.68
245	1.832712	37.936068	42.813	85.373	87.00	0.5015	2134.19	0.15	86.85	86.85
246	1.978403	-124.63983	23.119	61.901	114.63	0.3735	2008.32	0.86	113.77	66.23
252	2.835756	82.289044	7.072	28.773	29.17	0.2458	1452.55	0.46	28.71	28.71
249	2.893571	-83.974313	15.739	29.384	87.43	0.5356	1463.63	179.86	92.43	87.57

Object_ID	Latitude	Longitude	Width	Length	Feature_ Orientation	Aspect_ ratio	Sigma1 _max_kPa	Stress_ orientation	Orientation_ Diff_ 0-180	Orientation_ Diff_ 0-90
251	3.015183	175.955355	7.074	18.221	38.84	0.3882	1845.51	14.11	24.73	24.73
254	3.696224	76.656434	12.289	20.748	160.58	0.5923	1543.63	1.11	159.47	20.53
256	4.652292	-61.322491	36.022	62.868	108.29	0.5730	1975.93	179.19	70.90	70.90
258	4.680722	151.102614	29.866	42.702	153.95	0.6994	2151.13	1.95	152.00	28.00
263	5.203063	-135.88034	61.710	96.342	148.54	0.6405	2115.57	1.60	146.94	33.06
262	5.446028	153.677764	39.409	76.330	65.84	0.5163	2112.30	3.02	62.82	62.82
270	6.094475	56.689436	58.396	95.801	7.38	0.6096	1973.70	2.10	5.28	5.28
269	6.236254	-161.88235	55.561	87.953	56.05	0.6317	1929.87	178.52	122.47	57.53
265	6.383795	171.924343	22.280	47.900	58.70	0.4651	1861.14	13.00	45.70	45.70
273	7.004097	-139.38648	72.090	101.506	29.41	0.7102	2113.26	0.92	28.49	28.49
272	7.828128	-146.18414	17.077	26.177	21.69	0.6524	2084.09	0.00	21.69	21.69
271	7.927481	26.146022	5.740	8.121	153.30	0.7068	2011.96	0.41	152.89	27.11
275	8.300384	-70.466006	56.666	80.794	133.66	0.7014	1742.58	178.88	45.22	45.22
286	8.519766	33.307326	90.908	216.581	137.04	0.4197	2075.97	179.38	42.34	42.34
274	8.636329	-124.65566	15.652	22.695	69.06	0.6897	1984.02	2.99	66.07	66.07
277	9.763515	-132.19584	13.818	33.026	36.04	0.4184	2064.39	2.29	33.75	33.75
276	10.013759	11.531932	4.549	6.596	170.05	0.6897	1812.02	174.31	4.26	4.26
279	10.328321	-126.0068	35.639	59.184	132.79	0.6022	1992.26	2.99	129.80	50.20
280	10.338639	-107.02506	51.340	83.574	90.37	0.6143	1610.40	4.14	86.23	86.23
283	10.749842	160.779815	41.364	59.631	5.82	0.6937	1958.23	7.14	1.32	1.32
281	11.274179	38.43006	8.721	14.121	135.22	0.6176	2068.87	2.20	133.02	46.98
287	11.450354	-156.15625	15.971	36.490	174.36	0.4377	1945.89	178.86	4.50	4.50
292	11.963681	-157.43709	48.304	94.811	144.40	0.5095	1921.77	177.57	33.17	33.17
288	12.003816	-151.66345	12.134	20.227	142.00	0.5999	1991.19	178.97	36.97	36.97
289	12.064465	99.446345	30.416	45.794	133.96	0.6642	1511.73	178.97	45.01	45.01
291	12.203126	117.670594	45.502	72.611	89.96	0.6267	1914.48	178.12	88.16	88.16
293	12.92369	-141.76477	51.029	75.125	65.01	0.6793	2044.57	2.74	62.27	62.27
307	13.359827	52.503465	229.922	394.687	47.12	0.5825	1985.82	2.70	44.42	44.42

Object_ID	Latitude	Longitude	Width	Length	Feature_ Orientation	Aspect_ ratio	Sigma1 _max_kPa	Stress_ orientation	Orientation_ Diff_ 0-180	Orientation_ Diff_ 0-90
296	15.499571	-138.85606	8.434	13.626	64.85	0.6190	2021.67	1.97	62.88	62.88
302	15.742698	174.076786	23.144	91.639	137.90	0.2526	1718.33	21.62	116.28	63.72
298	15.938764	47.115552	10.110	25.710	86.91	0.3932	2006.19	2.65	84.26	84.26
300	16.219274	8.471334	34.479	50.461	89.08	0.6833	1685.40	0.95	88.13	88.13
303	16.57747	28.5814	34.050	55.595	127.01	0.6125	1926.55	178.57	51.56	51.56
301	16.586071	-126.57747	13.531	20.552	75.51	0.6584	1940.95	4.11	71.40	71.40
309	18.047922	43.703304	15.126	23.461	84.15	0.6447	1981.67	3.66	80.49	80.49
311	18.365584	57.176189	33.483	168.591	112.31	0.1986	1870.92	3.70	108.61	71.39
310	18.677452	-117.33386	15.244	35.557	179.02	0.4287	1779.10	7.11	171.91	8.09
313	18.820112	-62.861922	52.822	111.100	64.07	0.4754	1838.62	176.62	112.55	67.45
312	19.10482	-21.041948	26.072	49.461	62.52	0.5271	1844.40	10.57	51.95	51.95
319	19.378427	25.943426	86.199	142.731	130.77	0.6039	1837.86	175.81	45.04	45.04
315	19.500466	85.689766	50.350	74.559	113.97	0.6753	1421.26	2.46	111.51	68.49
316	19.722372	-104.97841	43.372	137.487	105.00	0.3155	1551.58	5.62	99.38	80.62
317	19.918923	-131.76603	34.341	54.984	134.45	0.6246	1938.41	4.26	130.19	49.81
320	21.050718	-56.872694	12.130	22.636	91.45	0.5359	1909.33	179.31	87.86	87.86
322	21.525918	-151.34806	37.126	55.349	106.60	0.6708	1819.88	178.76	72.16	72.16
326	21.946762	-75.014095	28.216	40.538	126.57	0.6960	1583.99	177.80	51.23	51.23
321	21.961302	124.892442	4.829	11.466	75.67	0.4212	1924.09	178.24	102.57	77.43
323	22.21666	-47.552047	4.683	10.569	7.00	0.4430	1975.06	0.07	6.93	6.93
325	22.319569	123.905681	7.201	11.801	99.08	0.6102	1903.47	179.93	80.85	80.85
335	22.412685	9.849419	58.243	108.924	164.20	0.5347	1548.31	4.02	160.18	19.82
332	22.451714	140.247339	36.557	53.101	177.10	0.6884	1978.79	3.13	173.97	6.03
329	22.51947	-134.70738	21.300	32.013	48.63	0.6654	1904.23	2.44	46.19	46.19
330	22.735408	-166.18794	14.247	20.581	105.09	0.6922	1580.85	179.03	73.94	73.94
331	22.827267	-165.17024	17.628	30.115	81.41	0.5853	1593.45	171.92	90.51	89.49
333	22.836992	120.019459	43.429	66.549	93.32	0.6526	1849.31	177.86	84.54	84.54
334	23.359223	-117.9063	9.372	17.712	143.28	0.5291	1744.45	8.00	135.28	44.72

Object_ID	Latitude	Longitude	Width	Length	Feature_ Orientation	Aspect_ ratio	Sigma1 _max_kPa	Stress_ orientation	Orientation_ Diff_ 0-180	Orientation_ Diff_ 0-90
338	24.081519	94.20619	24.302	110.939	19.08	0.2191	1431.01	1.09	17.99	17.99
336	24.261326	174.045279	32.854	47.872	107.20	0.6863	1514.85	19.69	87.51	87.51
337	24.634572	24.386414	14.999	31.270	174.07	0.4797	1696.05	173.71	0.36	0.36
340	25.550208	18.312777	21.382	30.309	108.28	0.7055	1578.38	170.83	62.55	62.55
342	25.644295	-165.96613	25.762	55.476	17.08	0.4644	1506.00	170.81	153.73	26.27
343	26.009139	14.908114	36.542	56.428	149.20	0.6476	1516.91	172.00	22.80	22.80
341	26.180663	4.931492	9.024	13.526	120.80	0.6672	1406.83	7.60	113.20	66.80
345	26.883626	-173.92481	11.554	17.226	31.69	0.6707	1387.11	9.89	21.80	21.80
346	27.247561	43.987244	15.804	25.549	172.95	0.6186	1819.86	1.39	171.56	8.44
348	27.695996	-158.0551	36.970	57.692	49.19	0.6408	1568.14	175.79	126.60	53.40
355	29.848889	151.468392	40.899	58.813	36.62	0.6954	1694.98	10.78	25.84	25.84
354	29.934908	115.53112	43.126	77.535	84.48	0.5562	1691.77	177.37	92.89	87.11
357	30.097543	129.400599	29.451	54.609	164.88	0.5393	1814.67	0.90	163.98	16.02
356	30.253369	156.24281	28.422	40.449	20.49	0.7027	1611.52	12.76	7.73	7.73
361	30.431224	-161.2887	38.141	54.686	76.62	0.6975	1442.42	171.59	94.97	85.03
360	30.533007	138.12566	38.892	59.076	74.13	0.6583	1802.52	4.72	69.41	69.41
359	30.801193	-18.483808	25.158	35.797	78.10	0.7028	1498.75	15.22	62.88	62.88
363	31.406234	-115.47056	11.094	37.526	151.76	0.2956	1635.32	7.91	143.85	36.15
362	31.514431	-116.47648	11.334	26.306	166.58	0.4308	1646.09	7.20	159.38	20.62
367	31.64246	-132.13042	109.780	162.986	37.31	0.6736	1727.00	1.73	35.58	35.58
366	32.441987	-100.50066	44.585	90.244	141.83	0.4940	1462.24	7.65	134.18	45.82
369	33.68678	-147.78497	18.483	27.135	1.32	0.6812	1564.84	174.21	172.89	7.11
368	33.760436	-171.03799	5.532	8.867	88.71	0.6239	1186.86	171.53	82.82	82.82
372	34.358012	22.208298	47.575	75.676	169.42	0.6287	1399.93	170.91	1.49	1.49
371	34.442925	-74.591108	9.309	16.986	82.81	0.5480	1516.71	177.05	94.24	85.76
373	35.267732	-154.25904	28.884	43.115	39.83	0.6699	1425.59	171.00	131.17	48.83
376	36.171939	-3.03294	25.190	35.985	2.23	0.7000	1097.85	20.65	18.42	18.42
386	36.820049	53.631142	118.629	178.753	157.10	0.6637	1637.33	3.16	153.94	26.06

Object_ID	Latitude	Longitude	Width	Length	Feature_ Orientation	Aspect_ ratio	Sigma1 _max_kPa	Stress_ orientation	Orientation_ Diff_ 0-180	Orientation_ Diff_ 0-90
382	37.95934	-87.788829	40.665	62.778	97.10	0.6478	1413.47	0.40	96.70	83.30
383	38.052181	109.170318	40.239	80.343	122.32	0.5008	1530.94	179.46	57.14	57.14
381	38.242742	-98.969296	14.441	42.796	70.20	0.3374	1444.60	5.66	64.54	64.54
379	38.350227	-82.947604	6.392	13.015	84.55	0.4912	1432.36	179.30	94.75	85.25
390	40.066546	-74.475677	90.971	159.948	159.14	0.5688	1480.99	0.74	158.40	21.60
391	41.746112	168.547938	63.319	115.192	28.03	0.5497	1051.53	23.36	4.67	4.67
396	42.876459	69.111649	82.240	127.548	11.89	0.6448	1503.75	5.29	6.60	6.60
398	44.324487	-91.452299	58.386	101.864	42.74	0.5732	1414.98	2.57	40.17	40.17
400	46.141729	51.741319	42.476	69.388	127.60	0.6122	1483.65	178.34	50.74	50.74
401	46.7722	-145.62975	36.413	54.491	46.82	0.6682	1298.21	169.18	122.36	57.64
405	48.171784	119.367336	74.684	113.730	101.32	0.6567	1469.53	3.39	97.93	82.07
407	48.503664	-122.99814	63.919	104.129	84.27	0.6138	1464.06	179.47	95.20	84.80
408	48.769761	-156.32652	36.598	60.672	165.13	0.6032	1077.81	161.70	3.43	3.43
406	49.279151	-175.51041	9.596	15.651	111.23	0.6131	648.35	151.81	40.58	40.58
410	49.404816	5.207684	58.479	81.826	146.78	0.7147	677.18	148.79	2.01	2.01
409	50.304101	-48.288109	6.516	20.694	84.44	0.3149	1390.79	10.05	74.39	74.39
414	50.89067	49.410521	136.148	210.569	147.61	0.6466	1410.07	176.18	28.57	28.57
412	51.224858	0.656582	35.824	61.180	137.89	0.5856	561.04	38.86	99.03	80.97
413	52.291656	-81.257137	22.374	32.186	67.50	0.6952	1414.02	5.70	61.80	61.80
415	53.613342	-161.93267	16.107	23.697	9.94	0.6797	917.81	152.73	142.79	37.21
416	53.861734	117.335833	15.990	29.095	171.29	0.5496	1410.20	6.17	165.12	14.88
419	54.478667	74.838025	24.801	45.283	174.70	0.5477	1437.22	6.61	168.09	11.91
418	54.581355	96.556782	10.462	31.027	161.89	0.3372	1413.94	4.08	157.81	22.19
420	54.905659	91.136584	8.723	35.665	29.45	0.2446	1417.60	5.10	24.35	24.35
426	60.75976	-143.81911	28.740	40.018	19.63	0.7182	1204.64	159.76	140.13	39.87
427	61.318583	-120.14868	87.032	185.538	141.75	0.4691	1387.86	177.90	36.15	36.15
428	63.872507	-99.510074	16.778	25.102	39.80	0.6684	1423.69	1.83	37.97	37.97
432	75.512547	66.217645	61.529	98.214	8.10	0.6265	1409.09	173.84	165.74	14.26

Table S2. Measurements and modeled stress orientations for mountains.

Object_ID	Latitude	Longitude	Unit	Width	Length	Feature_ Orientation	Aspect_ ratio	Sigma3 _min_kPa	Stress_ orientation	Orientation_ Diff_ 0-180	Orientation_ Diff_ 0-90
1	-87.277917	-97.210466	Mu	57.823	161.505	65.81	0.3580	-1425.89	175.71	109.90	70.10
2	-85.982101	-30.533408	Ml	69.669	114.227	35.96	0.6099	-1412.47	109.07	73.11	73.11
5	-77.825779	-175.92711	Mu	37.033	59.134	119.67	0.6262	-1287.05	74.11	45.56	45.56
27	-75.560833	116.831098	Ml	93.905	132.223	125.85	0.7102	-1379.75	148.88	23.03	23.03
50	-73.067008	164.576647	Ml	76.648	116.568	134.00	0.6575	-1165.26	100.78	33.22	33.22
54	-70.218736	110.224887	Ml	27.843	120.526	43.48	0.2310	-1383.11	162.36	118.88	61.12
57	-69.781926	-46.77633	Ml	215.121	317.352	85.79	0.6779	-1279.55	146.52	60.73	60.73
59	-66.336279	116.152828	Mm	24.612	30.797	164.79	0.7992	-1357.29	163.36	1.43	1.43
60	-65.440412	-43.181596	Mu	15.092	25.811	127.82	0.5847	-1235.47	154.89	27.07	27.07
61	-65.064174	110.822707	Ml	152.832	269.885	16.72	0.5663	-1376.82	168.43	151.71	28.29
62	-62.386325	56.112817	Ml	38.766	117.459	56.47	0.3300	-1368.73	5.59	50.88	50.88
66	-52.887191	88.088819	Ml	78.996	114.516	106.82	0.6898	-1418.72	172.18	65.36	65.36
74	-50.975658	-31.862596	Ml	180.000	287.506	138.97	0.6261	-1211.35	161.51	22.54	22.54
77	-48.049827	23.870083	Mu	162.800	272.187	45.06	0.5981	-1092.68	18.08	26.98	26.98
80	-45.945236	-23.643547	Ml	154.856	325.767	108.44	0.4754	-1175.99	160.01	51.57	51.57
82	-43.826882	-124.76946	Mm	86.254	196.530	115.44	0.4389	-1527.9	178.67	63.23	63.23
87	-41.794307	102.926623	Ml	150.260	217.165	83.32	0.6919	-1457.35	1.03	82.29	82.29
84	-40.872934	-57.105046	Mu	34.228	61.057	46.83	0.5606	-1582.85	177.68	130.85	49.15
92	-39.588578	75.053626	Ml	113.979	121.866	70.94	0.9353	-1480.06	174.33	103.39	76.61
88	-39.054128	-59.245974	Mu	23.576	30.129	52.38	0.7825	-1606.4	179.33	126.95	53.05
96	-36.37745	158.783621	Ml	76.067	165.435	159.40	0.4598	-1379.66	164.27	4.87	4.87
98	-35.123479	149.917307	Mu	73.747	113.420	173.08	0.6502	-1555.74	167.53	5.55	5.55
106	-32.18964	121.28307	Mu	111.821	138.945	25.84	0.8048	-1715.04	2.16	23.68	23.68
105	-31.043197	41.803524	Mu	44.897	65.417	115.55	0.6863	-1722.37	0.15	115.40	64.60
113	-28.218323	-160.56631	Ml	178.841	419.458	108.09	0.4264	-1526.11	7.69	100.40	79.60
110	-28.061475	-125.20142	Mu	109.832	137.705	113.43	0.7976	-1769.5	176.52	63.09	63.09
108	-27.837429	124.30211	Mu	74.556	80.778	16.74	0.9230	-1816.34	0.09	16.65	16.65
112	-27.827152	-30.079933	Mu	75.358	137.642	1.78	0.5475	-1769.53	170.93	169.15	10.85
115	-26.15179	-68.651171	Mu	61.414	118.338	120.15	0.5190	-1669.01	1.94	118.21	61.79
111	-25.950282	105.690512	Mu	10.700	28.792	63.04	0.3716	-1574.31	2.2	60.84	60.84
114	-25.91865	-44.074109	Mu	50.263	84.164	8.97	0.5972	-1914.31	177.25	168.28	11.72

Object_ID	Latitude	Longitude	Unit	Width	Length	Feature_ Orientation	Aspect_ ratio	Sigma3 _min_kPa	Stress_ orientation	Orientation_ Diff_ 0-180	Orientation_ Diff_ 0-90
134	-24.602588	161.993174	Ml	232.375	559.815	50.88	0.4151	-1665.37	164.86	113.98	66.02
126	-24.317444	-63.040011	Mu	48.307	178.915	166.59	0.2700	-1780.87	1.46	165.13	14.87
119	-24.18946	-170.90172	Mu	67.932	116.064	38.73	0.5853	-1493.42	177.86	139.13	40.87
123	-23.670873	-24.874322	Mu	97.987	114.948	49.90	0.8524	-1803.44	169.36	119.46	60.54
118	-23.642895	123.835318	Mu	27.393	73.010	88.22	0.3752	-1878.99	0.35	87.87	87.87
125	-23.173613	65.708666	Ml	59.983	159.750	68.96	0.3755	-1695.5	172.88	103.92	76.08
129	-21.927414	102.695685	Ml	200.788	210.712	169.86	0.9529	-1538.48	3.17	166.69	13.31
128	-21.206764	-93.149674	Mu	82.729	228.927	128.11	0.3614	-1416.09	176.89	48.78	48.78
130	-21.028127	-109.76347	Ml	124.007	292.145	86.13	0.4245	-1632.83	173.98	87.85	87.85
131	-19.598405	109.732172	Mu	45.327	58.702	61.14	0.7721	-1690.47	2.32	58.82	58.82
135	-17.599956	-11.565914	Mu	37.909	48.613	96.66	0.7798	-1742.3	163.89	67.23	67.23
136	-17.37471	-60.919309	Mu	163.054	260.743	59.48	0.6253	-1898.52	2.06	57.42	57.42
137	-16.680064	-120.7051	Mu	206.188	280.423	21.30	0.7353	-1860.44	175.56	154.26	25.74
145	-12.297048	-71.059327	Mm	142.146	191.617	53.53	0.7418	-1715.73	1.54	51.99	51.99
141	-12.293985	-56.26449	Mu	62.232	106.454	52.08	0.5846	-2027.71	1.38	50.70	50.70
139	-11.997776	-14.7906	Mu	22.205	42.538	152.56	0.5220	-1881	167.51	14.95	14.95
143	-10.812529	-73.311124	Mm	17.055	112.262	58.75	0.1519	-1664.61	1.87	56.88	56.88
146	-10.671398	-134.35864	Mu	110.319	114.180	55.70	0.9662	-2067.81	178.78	123.08	56.92
149	-10.034371	-112.79976	Mu	95.388	213.162	80.81	0.4475	-1743.31	176.39	95.58	84.42
144	-9.52939	-81.590312	Mu	25.695	33.876	85.93	0.7585	-1493.58	0.99	84.94	84.94
153	-8.983535	87.874369	Ml	138.412	164.117	152.76	0.8434	-1407.51	178.41	25.65	25.65
152	-7.778459	114.661354	Ml	138.884	199.483	129.23	0.6962	-1869.88	1.08	128.15	51.85
155	-7.685305	-79.093804	Ml	69.509	199.181	159.27	0.3490	-1544.21	0.43	158.84	21.16
150	-7.113739	81.806797	Mm	14.149	23.376	72.88	0.6053	-1456.68	178.65	105.77	74.23
156	-5.363601	83.185547	Ml	2.499	6.606	36.51	0.3783	-1442.43	178.81	142.30	37.70
157	-5.324012	81.291998	Ml	91.067	120.706	62.82	0.7545	-1461.42	179.02	116.20	63.80
160	-4.700823	-63.371225	Ml	156.973	294.456	174.98	0.5331	-1926.02	0.78	174.20	5.80
159	-2.849875	90.901766	Ml	86.924	167.273	32.00	0.5197	-1412.22	179.68	147.68	32.32
162	-1.87784	96.278951	Ml	126.892	198.264	5.60	0.6400	-1467.44	0.1	5.50	5.50
163	-1.871644	-82.045847	Ml	126.306	286.006	21.10	0.4416	-1488.33	179.97	158.87	21.13
170	-1.215364	41.780744	Ml	176.558	444.143	169.65	0.3975	-2138	179.6	9.95	9.95

Object_ID	Latitude	Longitude	Unit	Width	Length	Feature_ Orientation	Aspect_ ratio	Sigma3 _min_kPa	Stress_ orientation	Orientation_ Diff_ 0-180	Orientation_ Diff_ 0-90
166	1.293893	12.897031	Mu	66.938	109.159	64.91	0.6132	-1893.21	179.25	114.34	65.66
169	2.05134	18.491594	Mu	107.111	178.653	179.20	0.5995	-1958.02	179.31	0.11	0.11
171	4.06007	144.303844	Mu	112.856	166.598	158.06	0.6774	-2210.7	0.96	157.10	22.90
172	6.937492	75.658564	Mm	59.316	70.730	28.42	0.8386	-1563.48	2.01	26.41	26.41
176	8.418486	98.127024	Mm	110.388	159.672	3.01	0.6913	-1488.41	179.09	176.08	3.92
178	9.079844	123.780575	Ml	118.813	190.443	151.29	0.6239	-2054.74	179.01	27.72	27.72
175	9.326025	146.840481	Mu	36.550	64.793	162.33	0.5641	-2154.42	2.9	159.43	20.57
177	11.26787	145.606425	Mu	26.096	30.138	176.47	0.8659	-2142.66	2.83	173.64	6.36
179	13.063242	144.310864	Mu	25.260	31.811	131.78	0.7941	-2125.14	2.52	129.26	50.74
181	13.346676	127.548699	Mu	33.887	88.218	12.38	0.3841	-2071.44	179.88	167.50	12.50
182	13.70007	-85.232255	Mu	89.712	247.719	48.07	0.3622	-1439.13	179.15	131.08	48.92
189	14.792054	-104.19375	Ml	152.784	293.962	4.16	0.5197	-1548.66	4.63	0.47	0.47
183	14.829658	-3.543404	Mu	85.524	140.387	97.09	0.6092	-1712.54	20.15	76.94	76.94
184	15.13985	28.141935	Mu	54.278	120.648	122.57	0.4499	-1946.31	178.25	55.68	55.68
188	15.31172	-127.65724	Mu	98.019	311.297	129.04	0.3149	-1964.7	3.32	125.72	54.28
190	16.143775	-67.235588	Ml	62.777	220.438	8.75	0.2848	-1778.43	177.25	168.50	11.50
191	17.53993	-44.893626	Mu	84.226	165.940	52.50	0.5076	-2066.06	1.39	51.11	51.11
187	17.920998	-55.526618	Mu	27.244	43.622	3.84	0.6245	-1972.84	178.06	174.22	5.78
192	18.6057	-89.202318	Ml	106.013	216.328	90.66	0.4901	-1413.17	1.92	88.74	88.74
197	21.893857	-48.31506	Mu	41.641	120.137	35.48	0.3466	-1975.99	179.6	144.12	35.88
202	22.226491	-67.104496	Ml	100.048	210.085	15.37	0.4762	-1728.81	176.46	161.09	18.91
201	22.384759	170.454432	Mu	39.630	202.058	155.74	0.1961	-1607.8	19.49	136.25	43.75
195	22.532651	-152.1196	Mu	15.420	19.441	68.90	0.7931	-1788.26	177.91	109.01	70.99
199	23.59903	-61.033652	Mu	65.956	141.405	123.56	0.4664	-1817	176.97	53.41	53.41
200	24.117644	92.638653	Mu	67.317	82.349	9.37	0.8175	-1421.95	0.45	8.92	8.92
203	25.306045	-83.646579	Mu	60.433	81.289	56.02	0.7434	-1448.63	179.2	123.18	56.82
207	25.980398	-98.78906	Ml	193.167	231.853	16.60	0.8331	-1453.19	4.2	12.40	12.40
208	26.381293	-126.4554	Mu	150.841	280.768	160.82	0.5372	-1803.46	5.77	155.05	24.95
210	30.374911	-32.389148	Mu	110.313	152.764	142.21	0.7221	-1714.79	9.7	132.51	47.49
212	31.095898	-7.146403	Mu	84.470	198.268	30.30	0.4260	-1319.21	21.68	8.62	8.62
211	32.505871	-163.00354	Mu	40.879	69.748	150.50	0.5861	-1352.2	169.42	18.92	18.92

Object_ID	Latitude	Longitude	Unit	Width	Length	Feature_ Orientation	Aspect_ ratio	Sigma3 _min_kPa	Stress_ orientation	Orientation_ Diff_ 0-180	Orientation_ Diff_ 0-90
215	34.345837	-73.072534	Ml	86.630	232.612	156.63	0.3724	-1536.03	178	21.37	21.37
213	34.556872	-31.593972	Mu	51.931	92.677	168.36	0.5603	-1594.58	11	157.36	22.64
216	37.57308	-10.797783	Mu	71.475	80.350	151.03	0.8896	-1158.21	20.48	130.55	49.45
218	39.002247	-40.802468	Mu	20.268	62.372	15.36	0.3250	-1572.23	6.05	9.31	9.31
222	39.145137	-2.829072	Mu	114.522	197.543	56.83	0.5797	-991.197	25.64	31.19	31.19
220	39.636815	-93.931092	Mu	36.130	72.866	162.99	0.4958	-1422.02	5	157.99	22.01
219	39.674745	-70.235895	Mu	45.582	70.427	156.13	0.6472	-1518.85	179.72	23.59	23.59
224	40.474614	-80.454714	Mu	101.496	273.820	57.53	0.3707	-1442.45	0.91	56.62	56.62
225	42.596013	-57.041199	Mu	98.172	240.664	146.63	0.4079	-1548.43	2.27	144.36	35.64
228	46.407312	-126.32459	Ml	121.814	217.072	77.93	0.5612	-1483.11	0.18	77.75	77.75
230	47.225103	-160.9805	Mu	51.778	117.188	174.70	0.4418	-1006.8	160.17	14.53	14.53
233	48.380564	-62.220793	Mu	75.386	192.898	13.17	0.3908	-1460.75	1.98	11.19	11.19
232	48.725058	-164.35781	Ml	70.862	118.424	9.22	0.5984	-909.11	156.63	147.41	32.59
234	49.579721	110.447471	Mu	126.669	166.827	132.08	0.7593	-1442.16	0.34	131.74	48.26
235	52.859776	152.949143	Mu	87.135	148.540	75.86	0.5866	-1105.39	23.29	52.57	52.57
237	54.455927	-119.9176	Mu	45.396	108.130	11.33	0.4198	-1421.74	178.22	166.89	13.11
238	55.117864	24.42664	Mu	54.220	122.612	139.03	0.4422	-1046.66	155.66	16.63	16.63
239	57.766158	106.522028	Ml	72.568	168.942	148.26	0.4295	-1402.4	7.18	141.08	38.92
240	59.170781	161.524448	Mu	105.203	161.017	64.92	0.6534	-919.506	35.71	29.21	29.21
241	60.389262	36.097892	Mu	12.314	66.095	162.88	0.1863	-1210.64	159.6	3.28	3.28
244	63.240548	-61.4958	Mu	131.523	205.638	176.95	0.6396	-1349.52	12.82	164.13	15.87
242	64.942543	-175.161	Mu	28.457	58.942	1.21	0.4828	-896.104	119.41	118.20	61.80
246	69.497049	-49.680481	Mu	71.465	210.255	36.52	0.3399	-1292.24	30.58	5.94	5.94
245	69.958937	-37.12435	Mu	60.114	144.221	172.54	0.4168	-1215.62	43.02	129.52	50.48
247	71.422318	40.517687	Mu	111.594	153.613	163.18	0.7265	-1306.34	154.26	8.92	8.92
249	74.124424	72.209129	Mu	97.214	197.559	17.09	0.4921	-1416.35	173.92	156.83	23.17
248	74.141548	158.9575	Mu	30.723	76.613	125.47	0.4010	-1210.96	66.61	58.86	58.86